# Application of the Multi-Scale Infrastructure for Chemistry and Aerosols version 0 (MUSICAv0) for air quality in Africa

Wenfu Tang[1], Louisa K. Emmons[1], Helen M. Worden[1], Rajesh Kumar[2], Cenlin He[2], Benjamin Gaubert[1], Zhonghua Zheng[3], Simone Tilmes[1], Rebecca R. Buchholz[1], Sara-Eva Martinez-Alonso[1], Claire Granier[4,5], Antonin Soulie[4], Kathryn McKain[5,6], Bruce C. Daube[7], Jeff Peischl[5,8], Chelsea Thompson[8], and Pieternel Levelt[1,9,10]

[1]Atmospheric Chemistry Observations & Modeling Laboratory, National Center for Atmospheric Research, Boulder, CO, USA

[2]Research Applications Laboratory, National Center for Atmospheric Research, Boulder, CO, USA

[3]Department of Earth and Environmental Sciences, The University of Manchester, Manchester M13 9PL, United Kingdom

[4]Laboratoire d'Aérologie, CNRS, Université de Toulouse, Toulouse, France
[5]Cooperative Institute for Research in Environmental Sciences (CIRES), University of Colorado, Boulder, CO, USA
[6]Global Monitoring Laboratory (GML), National Oceanic and Atmospheric Administration, Boulder, CO, USA
[7]Department of Earth and Planetary Sciences, Harvard University, Cambridge, MA, USA
[8]NOAA Chemical Sciences Laboratory, Boulder, CO, USA
[9]Royal Netherlands Meteorological Institute (KNMI), Utrechtseweg 297, 3730 AE De Bilt, the Netherlands
[10]University of Technology Delft, Mekelweg 5, 2628 CD Delft, the Netherlands

Correspondence: Wenfu Tang (wenfut@ucar.edu)

## Abstract

The Multi-Scale Infrastructure for Chemistry and Aerosols Version 0 (MUSICAv0) is a new community modeling infrastructure that enables the study of atmospheric composition and chemistry across all relevant scales. We develop a MUSICAv0 grid with Africa refinement (~28 km × 28 km over Africa). We evaluate the MUSICAv0 simulation for 2017 with in situ observations and compare the model results to satellite products over Africa. A simulation from the Weather Research and Forecasting model coupled with Chemistry (WRF-Chem), a regional model that is widely used in Africa studies, is also included in the analyses as a reference. Overall, the performance of MUSICAv0 is comparable to WRF-Chem. Both models underestimate carbon monoxide (CO) compared to in situ observations and satellite CO column retrievals from the Measurements of Pollution in the Troposphere (MOPITT) satellite instrument. MUSICAv0 tends to overestimate ozone ($O_3$), likely due to overestimated stratosphere-to-troposphere flux of ozone. Both models significantly underestimate fine particulate matter ($PM_{2.5}$) at two surface sites in East Africa. The MUSICAv0 simulation agrees better with aerosol optical depth (AOD) retrievals from the Moderate Resolution Imaging Spectroradiometer (MODIS) and tropospheric nitrogen dioxide

(NO$_2$) column retrievals from the Ozone Monitoring Instrument (OMI) than WRF-Chem. MUSICAv0 has a consistently lower tropospheric formaldehyde (HCHO) column than OMI retrievals. Based on model-satellite discrepancies between MUSICAv0 and WRF-Chem and MOPITT CO, MODIS AOD, and OMI tropospheric NO$_2$, we find that future field campaign(s) and more in situ observations in an East African region (30°E – 45°E, 5°S – 5°N) could substantially improve the predictive skill of atmospheric chemistry model(s). This suggested focus region exhibits the largest model-in situ observation discrepancies, as well as targets for high population density, land cover variability, and anthropogenic pollution sources.

## 1. Introduction

As one of the most dramatically changing continents, Africa is experiencing myriad environmental sustainability issues (e.g., Washington et al., 2006; Ziervogel et al., 2014; Boone et al., 2016; Baudoin et al., 2017; Güneralp et al., 2017; Nicholson 2019; Fisher et al., 2021; Kumar et al., 2022). These environmental issues are causing vast losses in lives and in African economies, and are coupled with poverty and under-development (Washington et al., 2006; Fisher et al., 2021). Some of these environmental challenges are particularly severe in Africa compared to many other regions of the world (e.g., famine, droughts, floods, high temperatures, land degradation, and fires; Washington et al., 2006; van der Werf et al., 2017). However, even though Africa is the second largest continent, in land area and population, attention and research on environmental challenges in Africa are very limited, leading to a deficit of knowledge and solutions (e.g., De Longueville et al., 2010). Degraded air quality is an example of a severe environmental challenge with growing importance in Africa (e.g., Liousse et al., 2014; Thompson et al., 2014; Heft-Neal et al., 2018; Fisher et al., 2021; Vohra et al., 2022). A previous study found that air pollution across Africa caused ~1.1 million deaths in 2019 (Fisher et al., 2021). However, the study of air quality in Africa is hindered by the scarcity of ground-based observations (e.g., Paton-Walsh et al., 2022), modelling capability and the use of satellite observations. In this paper, we will focus on air quality analyses over Africa with the new model Multi-Scale Infrastructure for Chemistry and Aerosols (MUSICA; Pfister et al., 2020).

Atmospheric chemistry modeling is a useful tool to perform research on air quality conditions and evolution. Various models have been applied to study atmospheric chemistry and air quality in Africa such as the Weather Research and Forecasting (WRF) model coupled with Chemistry (WRF-Chem) (e.g., Kuik et al., 2015; Kumar et al., 2022), the GEOS-Chem chemical transport model (e.g., Marais et al., 2012, 2019; Lacey et al., 2018), the CHIMERE chemical transport model (e.g., Menut et al., 2018; Mazzeo et al., 2022), and the U.K. Earth System Model (UKESM1) (Brown et al., 2022), and GEOS5 (Bauer et al., 2019).

MUSICA is a new state-of-the-art community modeling infrastructure that enables the study of atmospheric composition and chemistry across all relevant scales (Pfister et al., 2020). The newly developed MUSICA Version 0 (MUSICAv0) is a global chemistry-climate model that allows global simulations with regional refinement down to a few kilometers spatial resolution (Schwantes et al., 2022). The coupling with other components of the Earth system (e.g., land, ocean, and sea ice) can also be performed at multiple scales. MUSICAv0 has various advantages and is particularly suitable for research applications over Africa. For example, MUSICAv0 can be used to study the interactions between atmospheric chemistry and other components of the Earth system and climate. MUSICA also includes the whole atmosphere (from the surface to thermosphere), and therefore can also be used to study the stratosphere and above and interactions between the stratosphere and troposphere. This is critical because some of the environmental issues

2

91    in Africa are coupled (e.g., the ozone–climate penalty; Brown et al., 2022). In addition, as a global
92    model, MUSICAv0 does not require boundary conditions to study a region at high resolution.
93    Global impacts and interactions can be simulated in a consistent and coherent way. This feature is
94    important as inflow from other continents and oceans significantly impacts air quality in Africa.
95    MUSICAv0 has been evaluated over North America (Schwantes et al., 2022, Tang et al., 2022)
96    and is also being developed and tested in other regions around the globe
97    (https://wiki.ucar.edu/display/MUSICA/Available+Grids).
98        This paper serves as the basis for the future application of MUSICAv0 in Africa. In this
99    study, we develop a MUSICAv0 model grid with regional refinement over Africa. Because
100   MUSICAv0 with Africa refinement is newly developed while WRF-Chem has been previously
101   used for African atmospheric chemistry and air quality studies, here we include results from WRF-
102   Chem to assess the ability of MUSICAv0 in reproducing the regional features of atmospheric
103   composition as simulated by WRF-Chem. We conduct the MUSICAv0 simulation for the year
104   2017 to compare with a previous WRF-Chem simulation (Kumar et al., 2022). MUSICAv0 and
105   the WRF-Chem simulation and the observational data used in this study are described in Section
106   2. The MUSICAv0 model simulation results are evaluated against in situ observations and
107   compared with satellite retrievals in Section 3. In Section 4, we provide an example application of
108   MUSICAv0 over Africa – identifying key potential regions in Africa for future in situ observations
109   and field campaign(s).
110
111   **2. Model and data**
112   **2.1 MUSICAv0**

113        MUSICA is a newly developed framework for simulations of large-scale atmospheric
114   phenomena in a global modeling framework, while still resolving chemistry at emission- and
115   exposure-relevant scales (Pfister et al., 2020). MUSICA version 0 (MUSICAv0) is a configuration
116   of the Community Earth System Model (CESM). It is also known as the Community Atmospheric
117   Model with chemistry (CAM-chem) (Tilmes et al., 2019; Emmons et al., 2020) with regional
118   refinement (RR) down to a few kilometers (Lauritzen et al., 2018; Schwantes et al., 2022). CAM-
119   chem, and thus MUSICAv0, includes several choices of chemical mechanisms of varying
120   complexity. This study uses the default MOZART-TS1 chemical mechanism for gas phase
121   chemistry (including comprehensive tropospheric and stratospheric chemistry; Emmons et al.,
122   2020) and the four-mode version of the Modal Aerosol Module (MAM4; Liu et al., 2016) for the
123   aerosol scheme. The MUSICAv0 model source code and the model documentation can be
124   downloaded through https://wiki.ucar.edu/display/MUSICA/MUSICA+Home (last access: 3
125   April 2023).

Moved (insertion) [1]

126        The MUSICAv0 users have the option to create their own model grid. MUSICAv0 is
127   currently being developed and tested for applications over various regions globally
128   (https://wiki.ucar.edu/display/MUSICA/Available+Grids), including North America, India, East
129   Asia, South America, Australia, and Korea, among others. (e.g., Schwantes et al., 2022; Tang et
130   al., 2022; Jo et al., 2023). In this study, we develop a model grid for applications in Africa
131   (ne0np4.africa_v5.ne30x4). As shown in Figure 1a, the horizontal resolution is ~111 km × 111 km
132   (i.e., 1° latitude × 1° equatorial longitude) globally, and ~28 km × 28 km (i.e., 0.25° latitude ×
133   0.25° equatorial longitude) within the region over Africa. Our simulation uses the default option
134   for vertical layers (i.e., 32 layers from the surface to ~3.64 hPa).

135  Here we run MUSICAv0 with the model grid for Africa for the year 2017, saving 3-hourly
136  output. We use the Copernicus Atmosphere Monitoring Service Global Anthropogenic emissions,
137  (CAMS-GLOB-ANTH) version 5.1 (Soulie et al., 2023) for anthropogenic emissions and the
138  Quick Fire Emissions Dataset (QFED) for fire emissions (Darmenov and da Silva, 2013). CAMS-
139  GLOB-ANTH version 5.1 emissions can be found at https://eccad3.sedoo.fr/data (last access: 3
140  April 2023). QFED emissions can be found at
141  https://portal.nccs.nasa.gov/datashare/iesa/aerosol/emissions/QFED/ (last access: 3 April 2023).
142  Plume rise climatology is applied to fire emissions following Tang et al. (2022). In addition, we
143  also include open waste burning (https://www.acom.ucar.edu/Data/fire/; Wiedinmyer et al., 2014)
144  emissions in the simulation. The model has the option of a free-running atmosphere or nudging to
145  external meteorological reanalysis. In this simulation, only wind and temperature are nudged to
146  the Modern-Era Retrospective analysis for Research and Applications, Version 2 (MERRA-2;
147  Gelaro et al., 2017) with a relaxation time of 12 hours. MERRA-2 data can be found at
148  https://disc.gsfc.nasa.gov/datasets?project=MERRA-2 (last access: 3 April 2023).

149  We also added carbon monoxide (CO) tracers in the simulation to understand the source
150  and transport of air pollution. CO tracers in CAM-chem/MUSICAv0 are described in detail by
151  Tang et al. (2019). In this study we include tracers for 6 regions (North Africa, West Africa, East
152  Africa, Central Africa, Southern Africa, and the rest of the world) and 3 emission sources
153  separately (anthropogenic emissions, fire emissions, and open waste burning emissions). In total,
154  there are 18 tagged CO tracers.

155
156  **2.2 WRF-Chem**
157  The Weather Research and Forecasting (WRF) model coupled with Chemistry (WRF-
158  Chem) is a regional chemical transport model. It has been widely used for air quality studies in
159  Africa. In this study we use model results from a WRF-Chem simulation described by Kumar et
160  al. (2022). The WRF-Chem simulation has a grid spacing of 20 km, slightly higher than the
161  MUSICAv0 simulation, and the model domain is highlighted in Figure 1a. The simulation has 36
162  vertical levels from the surface to ~50 hPa. The WRF-Chem simulation uses the Model for Ozone
163  and Related Tracers-4 (MOZART-4) chemical mechanism (Emmons et al., 2010) for tropospheric
164  gas phase chemistry, and the Goddard Global Ozone Chemistry Aerosol Radiation and Transport
165  (GOCART) model (Chin et al., 2002) for aerosol processes. The European Centre for Medium
166  Range Weather Forecasts (ECMWF) global reanalysis (ERA-Interim) fields are used for initial
167  and boundary meteorology conditions, while another CAM-chem simulation is used for initial and
168  boundary chemical conditions (Kumar et al., 2022). The WRF-Chem simulation used the global
169  Emission Database for Atmospheric Research developed for Hemispheric Transport of Air
170  Pollution (EDGAR-HTAP v2) for anthropogenic emissions and the Fire Inventory from NCAR
171  version 1.5 (FINNv1.5) (Wiedinmyer et al., 2011) for fire emissions. The WRF-Chem output is
172  saved hourly, however we only use 3-hourly output to match the MUSICAv0 simulation.

173
174  **2.3 ATom**
175  The Atmospheric Tomography mission (ATom; Thompson et al. 2022) was designed to
176  study the impact of human-produced air pollution on greenhouse gases, chemically reactive gases,
177  and aerosols in remote ocean air masses. ATom data are available at
178  https://espoarchive.nasa.gov/archive/browse/atom (last access: 3 April 2023). During the project,
179  the DC-8 aircraft sampled the remote troposphere with continuous vertical profiles. There were
180  four seasonal deployments from the summer of 2016 through the spring of 2018. Here we compare

Moved (insertion) [2]

4

181    the MUSICAv0 simulation with observations from ATom-2 (January–February 2017) and ATom-
182    3 (September–October 2017). Since the ATom flight tracks were mostly outside the WRF-Chem
183    domain (Figure 1a), we do not compare the WRF-Chem simulation with ATom data. However,
184    we compare chemical species from the MUSICAv0 simulation to the 2-minute merged ATom
185    measurements globally to obtain a benchmark and broader understanding of MUSICAv0
186    performance both within and outside the refined region. The model output is saved along the ATom
187    aircraft flight tracks and with respect to the observational times at run time. Nitric oxide (NO) and
188    ozone ($O_3$) measurements from the NOAA Nitrogen Oxides and Ozone (NOyO3) instrument
189    (Bourgeois et al., 2020, 2021) and the merged CO data (from Quantum Cascade Laser System and
190    NOAA Picarro CO measurements) are used.
191
192    **2.4 IAGOS**
193          The In-service Aircraft for a Global Observing System (IAGOS) is a European research
194    infrastructure, and was developed for operations on commercial aircraft to monitor atmospheric
195    composition (Petzold et al., 2015). IAGOS data are available at https://www.iagos.org/iagos-data/
196    (last access: 3 April 2023). The IAGOS instrument package 1 measures CO, $O_3$, air temperature,
197    and water vapor (https://www.iagos.org/iagos-core-instruments/package1/). CO is measured by
198    infrared absorption using the gas filter correlation technique (Precision: ±5%, Accuracy: ±5 ppb)
199    while $O_3$ is measured by UV absorption at 253.7 nm (Precision: ±2%, Accuracy: ±2 ppb). We use
200    airborne measurements of CO, $O_3$, air temperature, and water vapor from IAGOS for model
201    evaluation. The locations of the IAGOS flight tracks over Africa are shown in Figure 1b. The
202    model results and IAGOS data comparisons are conducted separately for five African sub-regions
203    (defined in Figure 1b).
204
205    **2.5 Ozonesondes**
206          The ozonesonde is a balloon-borne instrument that measures atmospheric $O_3$ profiles
207    through the electrochemical concentration cell using iodine/iodide electrode reactions (Thompson
208    et al., 2017), with records of temperature, pressure, and relative humidity from standard
209    radiosondes. NASA/GSFC SHADOZ data are available at https://tropo.gsfc.nasa.gov/shadoz/ (last
210    access: 3 April 2023). We use ozonesonde data from Southern Hemisphere ADditional
211    OZonesondes (NASA/GSFC SHADOZ; Thompson et al., 2017; Witte et al., 2017, 2018).
212    Specifically, ozonesonde data from four sites are used (Figure 1b): Ascension (Ascension Island,
213    U.K.), Nairobi (Kenya), Irene (South Africa), and La Reunion (La Réunion Island, France). The
214    average $O_3$ measurement uncertainty ranged from 5–9% for the ozonsonde data used in this study.
215
216    **2.6 WDCGG**
217          Monthly surface CO measurements from the World Data Center for Greenhouse Gases
218    (WDCGG; operated by the Japan Meteorological Agency in collaboration with the World
219    Meteorological Organization) are used for model evaluation. WDCGG data are available at
220    https://gaw.kishou.go.jp/ (last access: 3 April 2023). Data from six sites are used (Figure 1b),
221    namely (Ascension Island, U.K.), Assekrem (Algeria; remote site located in Saharan desert),
222    Gobabeb (Namibia; located at the base of a linear sand dune, next to an interdune plain), Cape
223    Point (South Africa; site exposed to the sea on top of a cliff 230 meters above sea level), Izana
224    (Tenerife, Spain; located on the Island that is ~300 km west of the African coast), and Mare
225    (Seychelles; near an international airport).
226

**2.7 Surface PM$_{2.5}$**

At the U.S. embassies, regulatory-grade monitoring data are collected with Beta Attenuation Monitors (BAMs), using a federal equivalent monitoring method, with an accuracy within 10% of federal reference methods (Watson et al., 1998; U.S. EPA, 2016). These instruments are operated by the U.S. State Department and the U.S. EPA, and data are available through AirNow (https://www.airnow.gov/international/us-embassies-and-consulates/). We use the measurements at the U.S. embassy locations in Addis Ababa Central (Ethiopia, 9.06° N, 38.76° E) and Kampala (Uganda, 0.30° N, 32.59° E) for the year 2017 as references (Malings et al., 2020) to match our simulations. The raw data are made available hourly and for this study we use daily mean PM$_{2.5}$ for comparison with model simulations.

**2.8 MOPITT**

The Measurements of Pollution in the Troposphere (MOPITT) instrument on board the NASA Terra satellite provides both thermal-infrared (TIR) and near-infrared (NIR) radiance measurements since March 2000. MOPITT CO data can be accessed through https://search.earthdata.nasa.gov/search (last access: 3 April 2023). Retrievals of CO column density and vertical profiles are provided in a multispectral TIR–NIR joint product which has sensitivity to near-surface as well as free tropospheric CO (Deeter et al., 2011; Worden et al., 2010). Here we use the MOPITT Version 9 Level 2 CO column product (Deeter et al., 2022) over Africa to evaluate the MUSICAv0 and WRF-Chem simulations. MOPITT Version 9 has significant updates to the cloud detection algorithm and NIR calibration scheme. The MOPITT satellite pixel size is ~22 km × 22 km, and the overpass time is ~10:30 am local time in 2017. When comparing model outputs to MOPITT the recommended data quality filter is applied and model outputs are interpolated to the MOPITT retrievals in space and time. To perform quantitative comparisons, the MOPITT averaging kernel and a priori are used to transform the model CO profiles to derive model column amounts.

**2.9 OMI NO$_2$ (QA4ECV)**

Tropospheric column NO$_2$ from the Ozone Monitoring Instrument (OMI) on board Aura is compared to the model in this study. Specifically, the NO$_2$ product from the quality assurance for the essential climate variables (QA4ECV) project is used (Boersma et al., 2017a; Compernolle et al., 2020). OMI NO$_2$ data are available at https://www.temis.nl/qa4ecv/no2.html (last access: 3 April 2023). The satellite pixel size is ~13 km × 25 km, and the overpass time is ~1:40 pm local time in 2017. A data quality filter was applied following the Product Specification Document (Boersma et al., 2017b; processing_error_flag = 0, solar_zenith_angle < 80, snow_ice_flag < 10 or snow_ice_flag = 255, amf_trop/amf_geo > 0.2, and cloud_radiance_fraction_no20 <= 0.5). Model profiles were transformed using the provided tropospheric air mass factor (AMF) and averaging kernels.

**2.10 OMI HCHO (QA4ECV)**

We also use tropospheric column HCHO from OMI in this study. Similar to OMI NO$_2$, we also use OMI HCHO product from QA4ECV (De Smedt et al., 2017a). OMI HCHO data are available at https://www.temis.nl/qa4ecv/hcho.html (last access: 3 April 2023). A data quality filter was applied following the Product User Guide (De Smedt et al., 2017b; processing_error_flag = 0 and processing_quality_flag = 0). Model profiles were transformed using provided averaging kernels. We note that HCHO retrievals are subject to relatively large uncertainties compared to

278 other satellite products used in this study. Therefore, the comparisons between model results and
279 the OMI HCHO product only indicate the model-satellite discrepancies rather than determining
280 model deficiencies. In addition, the WRF-Chem simulation from Kumar et al. (2022) does not
281 include HCHO in the output and hence will not be compared.

282
283 **2.11 MODIS AOD**
284      The aerosol optical depth (AOD) product (550 nm) from the Moderate Resolution Imaging
285 Spectroradiometer (MODIS) on board Terra NASA Terra satellite is used. MODIS AOD data can
286 be accessed through https://search.earthdata.nasa.gov/search (last access: 3 April 2023).
287 Specifically, we used the MODIS Level 2 Collection 6.1 product (MOD04_L2; Levy et al., 2017).
288 Deep Blue Aerosol retrievals are used (Hsu et al., 2013; Levy et al., 2013) to include retrievals
289 over the desert. The MODIS satellite pixel size is ~1 km × 1 km, and the overpass time is ~10:30
290 am local time.

291
292 **3. Model comparisons with satellite data and evaluation with in situ observations**
293      Africa includes a wide range of environments and emissions source. Therefore, in this
294 section we separate the continent in five sub-regions for analysis following Kumar et al. (2022).
295 CO is a good tracer of anthropogenic and biomass burning emissions and modeled CO tracers are
296 used in this section to understand sources. Figure 2 shows the seasonal averages of CO column
297 distributions over Africa from MOPITT along with the MUSICAv0 and WRF-Chem biases. The
298 highest levels of CO in these maps are primarily associated with biomass burning, which moves
299 around the continent with season. Both MUSICAv0 and WRF-Chem simulations underestimate
300 the CO column compared to MOPITT (Figures 3a and 3b). Overall, MUSICAv0 agrees better with
301 the OMI tropospheric $NO_2$ column (Figure 3c) and MODIS AOD (Figure 3e) than WRF-Chem
302 (Figures 3d and 3f). The MUSICAv0 simulation overall has lower tropospheric HCHO column
303 than OMI in all regions and seasons (Figure 3g). Spatial distributions of model biases against the
304 OMI tropospheric $NO_2$ column, MODIS AOD, and OMI tropospheric HCHO column are included
305 in Figures S1–S3. In this section we compare the model results with satellite data and in situ
306 observations over sub-regions in Africa and oceans near Africa (Figure 1b).

307
308 **3.1 North Africa**
309      Over North Africa, both MUSICAv0 and WRF-Chem simulations underestimate the CO
310 column during 2017 (Figures 2 and 3). As shown by the tagged model CO tracers (Figure 4), CO
311 over North Africa is mainly driven by transport of CO from outside the continent and
312 anthropogenic emissions. The model underestimation compared to the MOPITT CO column is
313 consistent with the results of the comparisons with surface CO observations from WDCGG at the
314 two sites located in North Africa (Assekrem and Izana; Figures 5a and 5c). At the two surface
315 sites, the composition of source types and source regions are close to the composition of source
316 types and source regions of the column average over North Africa (Figure 4 and Figures S4 and
317 S5), hence the two sites are representative of the background conditions of North Africa.
318 Compared to MODIS AOD, WRF-Chem has a mean bias of 0.36 whereas MUSICAv0's mean
319 bias is 0.17 for 2017. The model AOD biases over North Africa are likely driven by dust. No
320 comparison is made with IAGOS $O_3$ in North Africa due to data availability.

321
322 **3.2 West Africa**

323       Over West Africa, fire and anthropogenic emissions are both important for CO pollutant
324  and fire impacts peak in DJF (December, January, and February). Compared to the MOPITT CO
325  column, the mean bias of MUSICAv0 and WRF-Chem for West Africa peak around February –
326  the dry season of the Northern Hemisphere (Figure 3). In February, the MUSICAv0 mean bias is
327  $-1.1\times10^{18}$ molecules/cm$^2$ and WRF-Chem mean bias is $-7.5\times10^{17}$ molecules/cm$^2$, which are likely
328  driven by fire emission sources (Figure 4). Model comparisons with IAGOS CO also show a
329  similar bias – both model simulations underestimate CO at all vertical levels. The underestimation
330  peaks during DJF and below 600 hPa (Figure 6). As for MODIS AOD, WRF-Chem has the mean
331  bias 0.69 whereas MUSICAv0's mean bias is 0.15, respectively. Similar to North Africa, the model
332  biases in AOD over West Africa are also likely driven by dust and biomass burning. We also
333  compare modeled O$_3$ with IAGOS O$_3$ observations (Figure 7).
334       Over West Africa, both models agree well with the IAGOS O$_3$ observations below 800 hPa
335  (mean bias ranges from -1 to -4 ppb). Above 800 hPa over West Africa, WRF-Chem
336  underestimates O$_3$ while MUSICAv0 overestimates O$_3$. Overall, MUSICAv0 consistently
337  overestimates O$_3$ above 800 hPa in all seasons while the direction of WRF-Chem bias changes
338  with seasons (Figure 7). When MUSICAv0 overestimates O$_3$, the bias is in general larger at the
339  higher altitude of the troposphere. The concentration of the model stratospheric ozone tracer, O3S,
340  is also larger at the higher altitude in DJF (Figure 9). The correlation of modeled O$_3$ and O3S is
341  0.54, and the correlations of O$_3$S and model O$_3$ bias (modeled O$_3$ minus IAGOS O$_3$) is 0.35 over
342  West Africa, implying the overestimation of O$_3$ in the upper troposphere could be partially driven
343  by too strong stratosphere-to-troposphere flux of ozone. Lightning NO emissions can also impact
344  O$_3$ in the upper troposphere. The MUSICAv0 simulation has somewhat (~3 times) higher lightning
345  NO emissions (Figure S6) compared to a standard CAM-chem simulation (not shown), therefore
346  the high ozone in the upper troposphere may be due to an over-estimate of lightning NO. Impacts
347  of lightning NO emissions on upper troposphere O$_3$ in MUSICAv0 will be investigated and
348  evaluated further in the future. A brief comparison with IAGOS measurements of air temperature
349  and water vapor profiles over West Africa as well as other sub-regions shows that MUSICAv0
350  overall agrees well with these meteorological variables (Figure S7).
351
352  **3.3 Central Africa**
353       Compared to MOPITT CO column, the mean bias of MUSICAv0 and WRF-Chem for
354  Central Africa varies with seasons (Figure 3) but peaks during the dry season in September
355  (MUSICAv0 mean bias of $-1.0\times10^{18}$ molecules/cm$^2$; WRF-Chem mean bias of $-1.2\times10^{18}$
356  molecules/cm$^2$). The tagged model CO tracers show that in September, local fire emissions are the
357  dominant driver of CO in Central Africa (Figure 4). Compared to the IAGOS CO profiles (Figure
358  6), both models have the largest bias over Central Africa among the sub-regions in Africa – mean
359  bias of MUSICAv0 and WRF-Chem are -46 ppb and -36 ppb, respectively. The high bias over
360  Central Africa mainly occurs during the fire season. In central Africa, both models also
361  underestimate NO$_2$ (mean biases of MUSICAv0 and WRF-Chem are $-1.5\times10^{14}$ and $-5.5\times10^{14}$
362  molecules/cm$^2$, respectively). The underestimations in both CO and NO$_2$ by the two model
363  simulations are likely driven by the underestimation in fire emissions. Indeed, the emission
364  estimates from the newest version of FINN (FINNv2.5; Wiedinmyer et al., 2023) are higher
365  compared to both QFED (used in the MUSICAv0 simulation) and FINNv1.5 (used in the WRF-
366  Chem simulation) in this region.
367       Model mean bias of HCHO ($-1.3\times10^{16}$ molecules/cm$^2$ for the whole 2017) over Central
368  Africa is the largest among the five regions (Figure 3). The spatial distribution of HCHO bias

8

369  (Figure S4) largely co-locates with the vegetation (Figure 8). Over the barren or sparsely vegetated
370  area in North Africa and along the west coast of Southern Africa, HCHO biases are relatively small
371  while over the vegetated area HCHO bias are relatively large. Over North Africa, the mean bias is
372  $-0.66 \times 10^{16}$ molecules/cm$^2$ for the whole 2017 whereas over the other four regions, the mean bias
373  ranges from $-0.93 \times 10^{16}$ molecules/cm$^2$ to $-1.31 \times 10^{16}$ molecules/cm$^2$ for the whole 2017. This
374  indicates that the negative bias in MUSICAv0 HCHO could be due to underestimated biogenic
375  emissions in the model. In addition, the underestimation of HCHO in Central Africa (Figure S4)
376  co-locates with the underestimation of CO during fire season (Figure S1), implying that fire
377  emissions may also contribute to the HCHO underestimation in MUSICAv0. It is important to
378  note that the uncertainty of OMI tropospheric HCHO column is relatively large compared to other
379  satellite products. Here the averaged retrieval uncertainty (random and systematic) is ~120%.
380      When compared to the IAGOS O$_3$ profiles over Central Africa (Figure 7), both models
381  agree well with the IAGOS O$_3$ observations below 800 hPa (mean bias ranges from -1 to -4 ppb).
382  Above 800 hPa, WRF-Chem underestimates O$_3$ while MUSICAv0 overestimates O$_3$. The
383  correlation of modeled O$_3$ and O3S is 0.67, and the correlations of O$_3$S and model O$_3$ bias is 0.50
384  over Central Africa, indicating O$_3$ overestimation in Central Africa are more likely to be impacted
385  by stratosphere-to-troposphere flux of ozone than that in West Africa.
386
387  **3.4 East Africa**
388      CO over East Africa is dominated by local emissions and inflow from outside the continent.
389  Fire and anthropogenic emissions contribute approximately the same to CO over East Africa
390  (Figure 4). Both MUSICAv0 and WRF-Chem simulations underestimate the CO column
391  compared to MOPITT (Figure 3), and the WRF-Chem simulation also underestimate the
392  tropospheric NO$_2$ column compared to OMI. The biases in CO column and tropospheric NO$_2$
393  column peak in September, likely driven by fire emissions (Figure 4).
394      Compared to IAGOS O$_3$ profiles over East Africa, biases of MUSICAv0 below 600 hPa
395  has a seasonal variation while over 600 hPa are consistently positive (Figure 7). The correlations
396  of O$_3$S and model O$_3$ bias against IAGOS data is 0.50 in the region. The correlations between O$_3$S
397  and model O$_3$ bias are highest over Central and East Africa compared to other regions, indicating
398  stratosphere influence are strongest in these two regions among the sub-regions. Central and East
399  Africa are relatively more mountainous therefore topography driven stratospheric intrusions might
400  be expected. The Nairobi ozonesonde site is located in East Africa (Figure 1b). When comparing
401  to the O$_3$ profiles from ozonesondes (Figure 9), MUSICAv0 overall overestimates O$_3$ in the
402  troposphere at the four sites while WRF-Chem tends to underestimate O$_3$ in the free troposphere
403  (below 200 hPa). The Nairobi site is an exception where both MUSICAv0 and WRF-Chem
404  simulations significantly overestimate O$_3$ in all seasons (mean bias of MUSICAv0 and WRF-
405  Chem below 200 hPa are 27 ppb and 20 ppb, respectively). Among the four ozonesonde sites,
406  correlations of model bias of O$_3$ and O$_3$S are highest at the Nairobi site (0.74) where the model
407  significantly overestimates O$_3$. The results of model-ozonesonde comparisons are consistent with
408  the results of model-IAGOS comparisons and indicate a potential issue in modeled stratosphere-
409  to-troposphere flux of ozone.
410      There are two surface PM$_{2.5}$ sites in East Africa (Addis Ababa and Kampala; Figure 1b).
411  Despite using different aerosol methods and emission inventories, both MUSICAv0 and WRF-
412  Chem underestimate surface PM$_{2.5}$ when compared to observations at the two sites (Figure 10).
413  The errors in PM$_{2.5}$ concentrations at the U.S. Embassy in Kampala are especially prominent.
414  However, both models approximate the variation of the PM$_{2.5}$ in both locations. Many factors

9

415  contribute to the inconsistency in the magnitude of modeled $PM_{2.5}$ concentrations. For instance,
416  emission inventories in this region require additional improvement. In Uganda, increasing motor
417  vehicle ownership and burning biomass for domestic energy use contribute to ambient $PM_{2.5}$ levels
418  (Clarke et al., 2022; Petkova et al., 2013). Detailed $PM_{2.5}$ composition measurements would also
419  help to pinpoint the cause of inaccuracies. In addition, model resolutions could also be a potential
420  reason for the underestimation.
421
**3.5 Southern Africa**

422
423  Among the five regions, MUSICAv0 has the lowest mean bias ($-3.2\times10^{17}$ molecules/$cm^2$
424  annually) over Southern Africa (Figure 3). WRF-Chem also has low mean bias and RMSE over
425  Southern Africa except for the months of September, October, and November (SON) period where
426  WRF-Chem has larger CO mean bias ($-6.2\times10^{17}$ molecules/$cm^2$) than MUSICAv0. Tagged model
427  CO tracers indicate that CO over Southern Africa is significantly impacted by CO emissions from
428  Central Africa, East Africa, Southern Africa, and inflow from outside the continent. As for the
429  source types, anthropogenic and fire emissions are both important and fire impacts peak in
430  September. There are two WDCGG sites located in Southern Africa (Figure 1b; Gobabeb and Cape
431  Point). When compared to surface CO observations from WDCGG, both models consistently
432  underestimate CO by up to 40% at most sites. The Cape Point site in Southern Africa is an
433  exception (Figure 5) where MUSICAv0 overestimates CO by 40 ppb (annual mean; and up to 78
434  ppb in May 2017). CO tracers in the model (Figures S4 and S5) show that CO at Cape Point is
435  mainly driven by anthropogenic CO emissions from Southern Africa. Therefore, the
436  overestimation of CO by MUSICAv0 should be due to the overestimation of anthropogenic
437  emissions from Southern Africa used in the model. As for $NO_2$, WRF-Chem underestimates
438  tropospheric $NO_2$ column in most regions except for Southern Africa (Figure 3). Over Southern
439  Africa, WRF-Chem overestimates $NO_2$ especially during June, July, and August (JJA).
440  MUSICAv0 also tends to overestimates $NO_2$ at the same location in JJA however the bias is not
441  as large as for WRF-Chem.
442  MUSICAv0 simulation overall has a lower mean bias (0.14 annually) than the WRF-Chem
443  simulation (mean bias of 0.31 annually) compared to MODIS AOD with Southern Africa being
444  the only exception (Figure 3). Over Southern Africa, MUSICAv0 overestimates AOD by ~0.21
445  annually (Figure 3) and the bias peaks in January (mean bias=0.45). This overestimation in AOD
446  over Southern Africa is not seen in WRF-Chem. It is likely that the MUSICAv0 overestimation in
447  AOD over Southern Africa is also due to biases in modeled dust as the AOD bias is co-located
448  with the only barren or sparsely vegetated area in Southern Africa (Figure 8 and Figure S3).
449  Over Southern Africa, MUSICAv0 tends to overestimate $O_3$ compared to IAGOS at all
450  levels at all seasons in 2017 (Figure 7). The concentration of O3S over Southern Africa is higher
451  than those over other regions. However, the correlation of O3S and model $O_3$ bias is lower than
452  other regions (0.13) indicating stratosphere-to-troposphere flux of ozone may not be the main
453  driver of $O_3$ bias over Southern Africa even though stratosphere-to-troposphere flux of ozone are
454  relatively strong in the region. The Irene ozonesonde site is located in Southern Africa (Figure 1b).
455  Compared to the ozonesonde $O_3$ profiles at the Irene site, however, the MUSICAv0 performance
456  has a seasonal variation (Figure 9e-9h). Compared to other ozonesonde sites, the correlation of
457  O3S and model $O_3$ bias over Southern Africa is lower (0.14) and MUSICAv0 agrees relatively well
458  with observations, which is consistent with the comparison results with IAGOS data (Figure 7).
459
**3.6 Oceans near Africa**

461   We compare the CO, NO, and $O_3$ from the MUSICAv0 simulation with measurements
462 from ATom-2 and ATom-3 in 2017 (Figure 1a) to provide a global benchmark. Measurements
463 made over the Atlantic Ocean and Pacific Ocean, and in January-February (Jan-Feb) and
464 September-October (Sep-Oct) are compared separately (Figures 11 and 12). The comparison was
465 made with data averaged into 10° latitude and 200 hPa bins. Overall, the model consistently
466 underestimates CO globally in both seasons. The underestimation of CO is a common issue in
467 atmospheric chemistry models and could be due to various reasons, including emissions,
468 deposition, and chemistry (e.g., Fisher et al., 2017; Shindell et al., 2006; Stein et al., 2014; Tilmes
469 et al., 2015; Tang et al., 2018; Gaubert et al., 2020). Specifically for our MUSICAv0 simulation
470 in this study, the model bias in CO is relatively large (up to 52 ppb) over the Northern Hemisphere
471 (especially at high latitude and near the surface) and small over the Southern Hemisphere (Figures
472 11 and 12). Over the Atlantic Ocean, the bias in CO is larger in September-October than Jan-Feb
473 in both the Northern Hemisphere (-30 ppb in Jan-Feb versus -34 ppb in Sep-Oct) and Southern
474 Hemisphere (-11 ppb in Jan-Feb versus -14 ppb in Sep-Oct). Over the Pacific Ocean, however, the
475 CO bias is similar for both time periods in the Northern Hemisphere (-30 ppb) while in the
476 Southern Hemisphere, the CO bias changes significantly from -8 ppb in Jan-Feb to -16 ppb in Sep-
477 Oct. The changes in CO bias over the Southern Hemisphere are likely due to seasonal change in
478 fire emissions. Overall, the mean biases (Figures 11 and 12) suggest that the simulation agrees
479 better with ATom observations in the Southern Hemisphere than in the Northern Hemisphere, and
480 in Jan-Feb than in Sep-Oct (Figures 11 and 12), consistent with Gaubert et al. (2016).
481   In both seasons and both hemispheres, the model in general overestimates $O_3$ in the
482 stratosphere/UTLS (upper troposphere and lower stratosphere) by up to 38 ppb (above 200 hPa).
483 In the troposphere (below 200 hPa), the model overall agrees well with the ATom data over the
484 Pacific Ocean in the Southern Hemisphere (in most cases the bias is less than ±5 ppb). However,
485 over the Atlantic Ocean in the Southern Hemisphere, MUSICAv0 tends to overestimate $O_3$,
486 especially in Jan-Feb. In the troposphere of the Northern Hemisphere, MUSICAv0 consistently
487 overestimates $O_3$ over both oceans and both seasons. The positive bias in $O_3$ decreases from the
488 upper troposphere towards the surface, indicating that the overestimation of $O_3$ in the troposphere
489 may be due to stratosphere-to-troposphere flux of ozone. This was also noted for other global
490 models (Bourgeois et al. 2021). As for NO, the model tends to overestimate NO above 200 hPa
491 (approximately the stratosphere and Upper Troposphere-Lower Stratosphere; UTLS) by up to 50
492 ppt. Overall, the NO biases can be either positive or negative depending on location and season.
493 The distributions of NO bias (Figures 11 and 12) do not show an overall spatial pattern, unlike
494 those for CO (which changes monotonically with latitude) or $O_3$ (which changes monotonically
495 with altitude).
496

497 **4. Model application: identifying key regions in Africa for future in situ observations and**
498 **field campaign(s)**
499   As a demonstration of the application of MUSICAv0, here we use the results of model-
500 satellite comparisons to identify potential regions where the atmospheric chemistry models need
501 to be improved substantially. More field campaigns and more in situ observations would not only
502 provide observational benchmark dataset to understand and improve the modeling capability in
503 the region, but would be also useful for the validation and calibration of satellite products. Here
504 we use Taylor score to quantify model-satellite discrepancies. Taylor score (Taylor, 2001) is
505 defined by

506
$$S = \frac{4(1+R)}{(\sigma_f + 1/\sigma_f)^2(1+R_0)}$$

507  where $\sigma_f$ is the ratio of $\sigma_f$ (standard deviation of the model) and $\sigma_r$ (standard deviation of
508  observations), R is correlation between model and observations, and $R_0$ is the maximum
509  potentially realizable correlation (=1 in this study). Taylor score ranges from 0 to 1 and a higher
510  Taylor score indicates better satellite-model agreement. To identify potential locations, we
511  separate the Africa continent into $5° \times 5°$ (latitude $\times$ longitude) pixels as shown in Figure 13. And
512  for each pixel, we calculate Taylor scores of MUSICAv0 compared to the three satellite Level 2
513  products (e.g., MOPITT CO column retrievals, OMI tropospheric $NO_2$ column retrievals, and
514  MODIS AOD) separately. And then three Taylor scores are summed up to obtain the total Taylor
515  score for MUSICAv0 (ranges from 0 to 3) as shown in Figures 13a-13e. A similar calculation is
516  conducted for WRF-Chem (Figures 13f-13j). Note that we did not include Taylor scores for HCHO
517  in the total Taylor score due to that (1) WRF-Chem simulations did not save HCHO output, and
518  (2) the HCHO retrievals have relatively high uncertainties (Taylor scores of MUSICAv0 compared
519  to OMI tropospheric HCHO column retrievals are provided separately in Figure S8).
520      Overall, both MUSICAv0 and WRF-Chem have low total Taylor scores in the 30°E – 45°E,
521  5°S – 5°N region in East Africa (a region of 15° longitude × 10° latitude) during MAM (March,
522  April, and May), JJA (June, July, and August), and SON (September, October, and November), as
523  highlighted in Figure 13, indicating relatively large model-satellite discrepancies in the region.
524  Moreover, this is also the region where the Nairobi ozonesonde site and the Kampala surface $PM_{2.5}$
525  site are located (Figure 1b). As discussed above, both MUSICAv0 and WRF-Chem significantly
526  overestimate $O_3$ (Figure 9) and largely underestimate $PM_{2.5}$ (Figure 10) in the region. More in situ
527  observations or future field campaigns in the region can substantially help in the understanding
528  model-satellite and model-in situ observation discrepancies and improving model performance.
529      The 30°E – 45°E, 5°S – 5°N region in East Africa is potentially a favorable location for
530  future field campaign(s) not only because of the large model-satellite and model-in situ observation
531  discrepancies, but also due to that the population density is high and landcover are diverse in the
532  region (Figure 8). The relatively high population density in the region indicates that improved air
533  quality modeling in the region can benefit a large population. And a diverse landcover indicates
534  more processes/environments can be sampled. CO tracers in the model (Figure 14) show that CO
535  over the region is mainly driven by both anthropogenic and fire emissions. Anthropogenic
536  emissions play a more important role in this region compared to East Africa in general (Figures 4
537  and 14). In terms of source regions, emissions from East Africa and inflow from outside the
538  continent are the dominant source, with some contributions from Central Africa. Note that the
539  source analyses using model tracers may be subject to uncertainties in the emission inventories.
540  As discussed above (e.g., Section 3.4), there might be missing sources in the region. Therefore, a
541  field campaign in the region can help address this issue.
542      We would like to point out that in this analysis, the key area is selected using 3 satellite
543  products/chemical species and two models. The Taylor score is a comprehensive measure of model
544  performance that accounts for variance and correlation, however, other models and types of
545  comparisons may provide different answers.
546
547  **5. Conclusions**
548      Africa is one of the most rapidly changing regions in the world and air pollution is a
549  growing issue at multiple scales over the continent. MUSICAv0 is a new community modeling
550  infrastructure that enables the study of atmospheric composition and chemistry across all relevant

12

551 scales. We developed a MUSICAv0 grid with Africa refinement (~28 km × 28 km over Africa and
552 ~110 km × 110 km for the rest of the world) and conducted the simulation for the year 2017. We
553 evaluated the model with in situ observations including ATom-2 and ATom-3 airborne
554 measurements of CO, NO, and $O_3$, IAGOS airborne measurements of CO and $O_3$, $O_3$ profiles from
555 ozonesondes, surface CO observations from WDGCC, and surface $PM_{2.5}$ observations from two
556 U.S. Embassy locations. We then compare MUSICAv0 with satellite products over Africa, namely
557 MOPITT CO column, MODIS AOD, OMI tropospheric $NO_2$ column, and OMI tropospheric
558 HCHO column. Results from a WRF-Chem simulation were also included in the evaluations and
559 comparisons as a reference. Lastly, as an application of the model, we identified potential African
560 regions for in situ observations and field campaign(s) based on model-satellite discrepancies
561 (quantified by Taylor score), with regard to model-in situ observation discrepancies, source
562 analyses, population, and land cover. The main conclusions are as follows.

563     (1) When comparing to ATom-2 and ATom-3, MUSICAv0 consistently underestimates
564     CO globally. Overall, the negative model bias increases with latitude from the Southern
565     Hemisphere to the Northern Hemisphere. MUSICAv0 also tends to overestimate $O_3$ in the
566     stratosphere/UTLS, and the positive model bias overall decreases with altitude.

567     (2) The MUSICAv0 biases in $O_3$ when compared to ATom, IAGOS, and ozonesondes are
568     likely driven by stratosphere-to-troposphere fluxes of $O_3$ and lightning NO emissions.

569     (3) Overall, the performance of MUSICAv0 and WRF-Chem are similar when compared
570     to the surface CO observations from six WDCGG sites in Africa.

571     (4) Both models have negative bias compared to the MOPITT CO column, especially over
572     Central Africa in September, which is likely driven by fires.

573     (5) Overall, MUSICAv0 agrees better with OMI tropospheric $NO_2$ column than WRF-
574     Chem.

575     (6) MUSICAv0 overall has a lower tropospheric HCHO column than OMI retrievals in all
576     regions and seasons. Biogenic and fire emissions are likely to be the main driver of this
577     disagreement.

578     (7) Over Africa, the MUSICAv0 simulation has smaller mean bias and RMSE compared
579     to MODIS AOD than the WRF-Chem simulation.

580     (8) The 30°E – 45°E, 5°S – 5°N region in East Africa is potentially a favorable location for
581     future field campaign(s) not only because of the large model-satellite and model-in situ
582     observation discrepancies, but also due to the population density, landcover, and pollution
583     source in this region.

584     Overall, the performance of MUSICAv0 is comparable to WRF-Chem. The
585 underestimation of CO is a common issue in atmospheric chemistry models such as MUSICAv0
586 and WRF-Chem. The overestimation of $O_3$ in MUSICAv0 is likely driven by too strong of
587 stratosphere-to-troposphere fluxes of $O_3$ and perhaps an over-estimate of lightning NO emissions,
588 however, future studies are needed to confirm and solve this issue. The significant underestimation
589 in surface $PM_{2.5}$ at two sites in East Africa and the overall overestimation in AOD in Africa
590 compared to MODIS imply missing local sources and an overestimation of dust emissions, and
591 require further study. Field campaigns and more in situ observations in 30°E–45°E, 5°S–5°N
592 region in East Africa are necessary for the improvement of atmospheric chemistry model(s) as

13

593 shown by the MUSICAv0 and WRF-Chem simulations. In the future, we plan to conduct a model
594 simulation for multiple years and develop additional model grids with potentially higher resolution
595 in Africa sub-regions based on the current MUSICAv0 Africa grid.

596

## Code and data availability

598 The model code used here can be accessed through https://doi.org/10.5281/zenodo.8051435. The
599 data produced by this study can be accessed through https://doi.org/10.5281/zenodo.8051443.

600

617

## Competing interests

619 The contact author has declared that neither they nor their co-authors have any competing
620 interests.

621

## Author contributions

623 WT, LKE, HMW, and PL were involved in the initial design of this study. WT led the analysis.
624 RK and CH conducted the WRF-Chem simulation. ZZ interpretated $PM_{2.5}$ results. BG, ST, SM
625 and other coauthors provide discussions. RRB helped with QFED emissions. CG and AS produced
626 CAMSv5.1 emissions. KM, BCD, JP, and CT conducted measurements during ATom. WT
627 prepared the paper with improvements from all coauthors.

628

629

## Reference

631 Baudoin, M.A., Vogel, C., Nortje, K. and Naik, M., 2017. Living with drought in South Africa:
632 lessons learnt from the recent El Niño drought period. International journal of disaster risk
633 reduction, 23, pp.128-137.

689  Bauer, S. E., Im, U., Mezuman, K., & Gao, C. Y. (2019). Desert dust, industrialization, and
690  agricultural fires: Health impacts of outdoor air pollution in Africa. *Journal of Geophysical*
691  *Research: Atmospheres*, 124, 4104– 4120. https://doi.org/10.1029/2018JD029336.

692  Boone, A.A., Xue, Y., De Sales, F., Comer, R.E., Hagos, S., Mahanama, S., Schiro, K., Song, G.,
693  Wang, G., Li, S. and Mechoso, C.R., 2016. The regional impact of Land-Use Land-cover Change
694  (LULCC) over West Africa from an ensemble of global climate models under the auspices of the
695  WAMME2 project. Climate Dynamics, 47(11), pp.3547-3573.

696  Brown, F., Folberth, G. A., Sitch, S., Bauer, S., Bauters, M., Boeckx, P., Cheesman, A. W., Deushi,
697  M., Dos Santos Vieira, I., Galy-Lacaux, C., Haywood, J., Keeble, J., Mercado, L. M., O'Connor,
698  F. M., Oshima, N., Tsigaridis, K., and Verbeeck, H., 2022. The ozone–climate penalty over South
699  America and Africa by 2100, Atmos. Chem. Phys., 22, 12331–12352, https://doi.org/10.5194/acp-
700  22-12331-2022.
701
702  Boersma, K. F., Eskes, H., Richter, A., De Smedt, I., Lorente, A., Beirle, S., Van Geffen, J., Peters,
703  E., Van Roozendael, M. and Wagner, T., (2017a). QA4ECV NO2 tropospheric and stratospheric
704  vertical column data from OMI (Version 1.1). Royal Netherlands Meteorological Institute
705  (KNMI). http://doi.org/10.21944/qa4ecv-no2-omi-v1.1.
706
707  Boersma, K.F., van Geffen, J., Eskes, H., van der A, R., De Smedt, I. and Van Roozendael, M.,
708  2017b. Product specification document for the QA4ECV NO2 ECV precursor product.
709
710  Bourgeois, I., Peischl, J., Thompson, C. R., Aikin, K. C., Campos, T., Clark, H., Commane, R.,
711  Daube, B., Diskin, G. W., Elkins, J. W., Gao, R.-S., Gaudel, A., Hintsa, E. J., Johnson, B. J., Kivi,
712  R., McKain, K., Moore, F. L., Parrish, D. D., Querel, R., Ray, E., Sánchez, R., Sweeney, C.,
713  Tarasick, D. W., Thompson, A. M., Thouret, V., Witte, J. C., Wofsy, S. C., and Ryerson, T. B.:
714  Global-scale distribution of ozone in the remote troposphere from the ATom and HIPPO airborne
715  field missions, Atmos. Chem. Phys., 20, 10611–10635, https://doi.org/10.5194/acp-20-10611-
716  2020, 2020.
717
718  Bourgeois, I., Peischl, J., Neuman, J.A., Brown, S.S., Thompson, C.R., Aikin, K.C., Allen, H.M.,
719  Angot, H., Apel, E.C., Baublitz, C.B. and Brewer, J.F., 2021. Large contribution of biomass
720  burning emissions to ozone throughout the global remote troposphere. Proceedings of the National
721  Academy of Sciences, 118(52), p.e2109628118.
722
723  Center for International Earth Science Information Network (CIESIN), Columbia University.
724  2018. Documentation for the Gridded Population of the World, Version 4 (GPWv4), Revision 11
725  Data Sets. Palisades NY: NASA Socioeconomic Data and Applications Center (SEDAC).
726  https://doi.org/10.7927/H45Q4T5F Accessed 2022-11-17.

727  Chin, M., Ginoux, P., Kinne, S., Torres, O., Holben, B.N., Duncan, B.N., Martin, R.V., Logan,
728  J.A., Higurashi, A., Nakajima, T., 2002. Tropospheric aerosol optical thickness from the GOCART
729  model and comparisons with satellite and sun photometer measurements. J. Atmos. Sci. 59, 461–
730  483. https://doi.org/10.1175/ 1520-0469(2002)059<0461:TAOTFT>2.0.CO;2.

15

731 Clarke, K., Ash, K., Coker, E.S., Sabo-Attwood, T. and Bainomugisha, E., 2022. A Social
732 Vulnerability Index for Air Pollution and Its Spatially Varying Relationship to PM2. 5 in Uganda.
733 Atmosphere, 13(8), p.1169.

734 Compernolle, S., Verhoelst, T., Pinardi, G., Granville, J., Hubert, D., Keppens, A., Niemeijer, S.,
735 Rino, B., Bais, A., Beirle, S., Boersma, F., Burrows, J. P., De Smedt, I., Eskes, H., Goutail, F.,
736 Hendrick, F., Lorente, A., Pazmino, A., Piters, A., Peters, E., Pommereau, J.-P., Remmers, J.,
737 Richter, A., van Geffen, J., Van Roozendael, M., Wagner, T., and Lambert, J.-C.: Validation of
738 Aura-OMI QA4ECV $NO_2$ climate data records with ground-based DOAS networks: the role of
739 measurement and comparison uncertainties, Atmos. Chem. Phys., 20, 8017–8045,
740 https://doi.org/10.5194/acp-20-8017-2020, 2020.

741 Darmenov, A., & da Silva, A. (2013). The quick fire emissions dataset (QFED)–documentation of
742 versions 2.1, 2.2 and 2.4. NASA Technical Report Series on Global Modeling and Data
743 Assimilation, NASA TM-2013-104606, 32, 183.

744 De Longueville, F., Hountondji, Y.C., Henry, S. and Ozer, P., 2010. What do we know about
745 effects of desert dust on air quality and human health in West Africa compared to other regions?.
746 Science of the total environment, 409(1), pp.1-8.

747 De Smedt, I., Yu, H., Richter, A., Beirle, S., Eskes, H., Boersma, K.F., Van Roozendael, M., Van
748 Geffen, J., Lorente, A. and Peters, E., (2017a), QA4ECV HCHO tropospheric column data from
749 OMI (Version 1.1). Royal Belgian Institute for Space Aeronomy.
750 http://doi.org/10.18758/71021031.

751 De Smedt, I., Van Geffen, J., Richter, A., Beirle S., Yu, H., Vlietinck J., Van Roozendael, M. van
752 der A R., Lorente A., Scanlon T., Compernolle S., Wagner T., Boersma, K. F., Eskes, H., 2017b,
753 Product User Guide for HCHO.

754 Deeter, M.N., 2009. MOPITT (Measurements of Pollution in the Troposphere) Validated Version
755 4 Product User's Guide. National Centre for Atmospheric Research, Boulder, CO, 80307.

756 Deeter, M. N.,Worden, H. M., Gille, J. C., Edwards, D. P.,Mao, D., and Drummond, J. R.:
757 MOPITT multispectral CO retrievals: Origins and effects of geophysical radiance errors, J.
758 Geophys. Res., 116, D15303, https://doi.org/10.1029/2011JD015703, 2011.

759 Deeter, M., Francis, G., Gille, J., Mao, D., Martínez-Alonso, S., Worden, H., Ziskin, D.,
760 Drummond, J., Commane, R., Diskin, G., and McKain, K.: The MOPITT Version 9 CO product:
761 sampling enhancements and validation, Atmos. Meas. Tech., 15, 2325–2344,
762 https://doi.org/10.5194/amt-15-2325-2022, 2022.

763 Emmons, L.K., Walters, S., Hess, P.G., Lamarque, J.-F., Pfister, G.G., Fillmore, D., Granier, C.,
764 Guenther, A., Kinnison, D., Laepple, T., Orlando, J., Tie, X., Tyndall, G., Wiedinmyer, C.,
765 Baughcum, S.L., Kloster, S., 2010. Description and evaluation of the model for ozone and related
766 chemical tracers, version 4 (MOZART-4). Geosci. Model Dev. 3, 43–67.
767 https://doi.org/10.5194/gmd-3-43-2010.

768  Emmons, L.K., Schwantes, R. H., Orlando, J. J., Tyndall, G., Kinnison, D., Lamarque, J.-F., et al.:
769  The Chemistry Mechanism in the Community Earth System Model version 2 (CESM2), Journal
770  of Advances in Modeling Earth Systems, 12, https://doi.org/10.1029/2019MS001882, 2020.

771  Fisher, J. A., Murray, L. T., Jones, D. B. A., & Deutscher, N. M. (2017). Improved method for
772  linear carbon monoxide simulation and source attribution in atmospheric chemistry models
773  illustrated using GEOS-Chem v9. Geoscientific Model Development, 10, 4129–4144.
774  https://doi.org/10.5194/gmd-10-4129-2017.

775  Fisher, S., Bellinger, D.C., Cropper, M.L., Kumar, P., Binagwaho, A., Koudenoukpo, J.B., Park,
776  Y., Taghian, G. and Landrigan, P.J., 2021. Air pollution and development in Africa: impacts on
777  health, the economy, and human capital. The Lancet Planetary Health, 5(10), pp.e681-e688.

778  Friedl, M., D. Sulla-Menashe. MODIS/Terra+Aqua Land Cover Type Yearly L3 Global 0.05Deg
779  CMG  V061.  2022,  distributed  by  NASA  EOSDIS  Land  Processes  DAAC,
780  https://doi.org/10.5067/MODIS/MCD12C1.061. Accessed 2022-11-17.

781  Gaubert, B., Arellano, A. F., Barré, J., Worden, H. M., Emmons, L. K., Tilmes, S., Buchholz, R.
782  R., Vitt, F., Raeder, K., Collins, N., Anderson, J. L., Wiedinmyer, C., Martínez-Alonso, S.,
783  Edwards, D. P., Andreae, M. O., Hannigan, J. W., Petri, C., Strong, K., and Jones, N.: Toward a
784  chemical reanalysis in a coupled chemistry-climate model: An evaluation of MOPITT CO
785  assimilation and its impact on tropospheric composition, J. Geophys. Res.-Atmos., 121, 7310–
786  7343, https://doi.org/10.1002/2016JD024863, 2016.

787  Gaubert, B., Emmons, L. K., Raeder, K., Tilmes, S., Miyazaki, K., Arellano Jr., A. F., Elguindi,
788  N., Granier, C., Tang, W., Barré, J., Worden, H. M., Buchholz, R. R., Edwards, D. P., Franke, P.,
789  Anderson, J. L., Saunois, M., Schroeder, J., Woo, J.-H., Simpson, I. J., Blake, D. R., Meinardi, S.,
790  Wennberg, P. O., Crounse, J., Teng, A., Kim, M., Dickerson, R. R., He, H., Ren, X., Pusede, S. E.,
791  and Diskin, G. S.: Correcting model biases of CO in East Asia: impact on oxidant distributions
792  during KORUS-AQ, Atmos. Chem. Phys., 20, 14617–14647, https://doi.org/10.5194/acp-20-
793  14617-2020, 2020.

794  Gelaro, R., McCarty, W., Suárez, M. J., Todling, R., Molod, A., Takacs, L., et al. (2017). The
795  modern-era retrospective analysis for research and applications, version 2 (MERRA-2). Journal of
796  Climate, 30(14), 5419-5454.

797  Güneralp, B., Lwasa, S., Masundire, H., Parnell, S. and Seto, K.C., 2017. Urbanization in Africa:
798  challenges and opportunities for conservation. Environmental research letters, 13(1), p.015002.

799  Heft-Neal, S., Burney, J., Bendavid, E. and Burke, M., 2018. Robust relationship between air
800  quality and infant mortality in Africa. Nature, 559(7713), pp.254-258.

801  Hsu, N.C., Jeong, M.J., Bettenhausen, C., Sayer, A.M., Hansell, R., Seftor, C.S., Huang, J. and
802  Tsay, S.C., 2013. Enhanced Deep Blue aerosol retrieval algorithm: The second generation. Journal
803  of Geophysical Research: Atmospheres, 118(16), pp.9296-9315.

804   Jo, D., et al., Effects of Grid Resolution and Emission Inventory on Urban Air Quality Simulation
805   With the Multi-Scale Infrastructure for Chemistry and Aerosols (MUSICA) Version 0, JAMES,
806   in review, 2022.

807   Kuik, F., Lauer, A., Beukes, J. P., Van Zyl, P. G., Josipovic, M., Vakkari, V., Laakso, L., and Feig,
808   G. T.: The anthropogenic contribution to atmospheric black carbon concentrations in southern
809   Africa: a WRF-Chem modeling study, Atmos. Chem. Phys., 15, 8809–8830,
810   https://doi.org/10.5194/acp-15-8809-2015, 2015.

811   Kumar, R., He, C., Bhardwaj, P., Lacey, F., Buchholz, R.R., Brasseur, G.P., Joubert, W.,
812   Labuschagne, C., Kozlova, E. and Mkololo, T., 2022. Assessment of regional carbon monoxide
813   simulations over Africa and insights into source attribution and regional transport. Atmospheric
814   Environment, 277, p.119075.

815   Lacey, F. G., Marais, E. A., Henze, D. K., Lee, C. J., van Donkelaar, A., Martin, R. V., et al. (2017).
816   Improving present day and future estimates of anthropogenic sectoral emissions and the resulting
817   air quality impacts in Africa. Faraday Discussions, 200, 397–412.
818   https://doi.org/10.1039/C7FD00011A.

819   Lauritzen, P. H., Nair, R. D., Herrington, A. R., Callaghan, P., Goldhaber, S., Dennis, J. M.,
820   Bacmeister, J. T., Eaton, B. E., Zarzycki, C. M., Taylor, M. A., Ullrich, P. A., Dubos, T., Gettelman,
821   A., Neale, R. B., Dobbins, B., Reed, K. A., Hannay, C., Medeiros, B., Benedict, J. J. and Tribbia,
822   J. J.: NCAR Release of CAM-SE in CESM2.0: A Reformulation of the Spectral Element
823   Dynamical Core in Dry-Mass Vertical Coordinates With Comprehensive Treatment of
824   Condensates and Energy, Journal of Advances in Modeling Earth Systems, 10(7), 1537–1570,
825   2018.

826   Levy, R. C., Mattoo, S., Munchak, L. A., Remer, L. A., Sayer, A. M., Patadia, F., and Hsu, N. C.:
827   The Collection 6 MODIS aerosol products over land and ocean, Atmos. Meas. Tech., 6, 2989–
828   3034, https://doi.org/10.5194/amt-6-2989-2013, 2013.

829   Levy, R., Hsu, C., et al., 2017. MODIS Atmosphere L2 Aerosol Product. NASA MODIS Adaptive
830   Processing System, Goddard Space Flight Center, USA:
831   http://dx.doi.org/10.5067/MODIS/MOD04_L2.061.

832   Liousse, C., Assamoi, E., Criqui, P., Granier, C., and Rosset, R.: Explosive growth in African
833   combustion emissions from 2005 to 2030, Environ. Res. Lett., 9, 35003,
834   https://doi.org/10.1088/1748-9326/9/3/035003, 2014.

835   Liu, J. C., Mickley, L. J., Sulprizio, M. P., Dominici, F., Yue, X., Ebisu, K., ... & Bell, M. L. (2016).
836   Particulate air pollution from wildfires in the Western US under climate change. Climatic change,
837   138(3), 655-666.

838   Malings, C., Westervelt, D. M., Hauryliuk, A., Presto, A. A., Grieshop, A., Bittner, A., Beekmann,
839   M., and R. Subramanian: Application of low-cost fine particulate mass monitors to convert satellite
840   aerosol optical depth to surface concentrations in North America and Africa, Atmos. Meas. Tech.,
841   13, 3873–3892, https://doi.org/10.5194/amt-13-3873-2020, 2020.

842 Marais, E. A., Jacob, D. J., Kurosu, T. P., Chance, K., Murphy, J. G., Reeves, C., Mills, G., Casadio,
843 S., Millet, D. B., Barkley, M. P., Paulot, F., and Mao, J.: Isoprene emissions in Africa inferred
844 from OMI observations of formaldehyde columns, Atmos. Chem. Phys., 12, 6219–6235,
845 https://doi.org/10.5194/acp-12-6219-2012, 2012.

846 Marais, E.A., Silvern, R.F., Vodonos, A., Dupin, E., Bockarie, A.S., Mickley, L.J. and Schwartz,
847 J., 2019. Air quality and health impact of future fossil fuel use for electricity generation and
848 transport in Africa. Environmental science & technology, 53(22), pp.13524-13534.

849 Mazzeo, A., Burrow, M., Quinn, A., Marais, E. A., Singh, A., Ng'ang'a, D., Gatari, M. J., and Pope,
850 F. D.: Evaluation of the WRF and CHIMERE models for the simulation of PM2.5 in large East
851 African urban conurbations, Atmos. Chem. Phys., 22, 10677–10701, https://doi.org/10.5194/acp-
852 22-10677-2022, 2022.

853 Menut, L., Flamant, C., Turquety, S., Deroubaix, A., Chazette, P., and Meynadier, R.: Impact of
854 biomass burning on pollutant surface concentrations in megacities of the Gulf of Guinea, Atmos.
855 Chem. Phys., 18, 2687–2707, https://doi.org/10.5194/acp-18-2687-2018, 2018.

856 Nicholson, S.E., 2019. A review of climate dynamics and climate variability in Eastern Africa.
857 The limnology, climatology and paleoclimatology of the East African lakes, pp.25-56.

858 Paton-Walsh, C., Emmerson, K.M., Garland, R.M., Keywood, M., Hoelzemann, J.J., Huneeus, N.,
859 Buchholz, R.R., Humphries, R.S., Altieri, K., Schmale, J. and Wilson, S.R., 2022. Key challenges
860 for tropospheric chemistry in the Southern Hemisphere. Elem Sci Anth, 10(1), p.00050.

861 Petkova, E.P., Jack, D.W., Volavka-Close, N.H. and Kinney, P.L., 2013. Particulate matter
862 pollution in African cities. Air Quality, Atmosphere & Health, 6(3), pp.603-614.

863 Petzold, A., Thouret, V., Gerbig, C., Zahn, A., Brenninkmeijer, C.A., Gallagher, M., Hermann,
864 M., Pontaud, M., Ziereis, H., Boulanger, D. and Marshall, J., 2015. Global-scale atmosphere
865 monitoring by in-service aircraft–current achievements and future prospects of the European
866 Research Infrastructure IAGOS. Tellus B: Chemical and Physical Meteorology, 67(1), p.28452.

867 Pfister, G. G., Eastham, S. D., Arellano, A. F., Aumont, B., Barsanti, K. C., Barth, M. C., ... &
868 Brasseur, G. P. (2020). The Multi-Scale Infrastructure for Chemistry and Aerosols (MUSICA).
869 Bulletin of the American Meteorological Society, 101(10), E1743-E1760.

870 Schwantes, R.H., Lacey, F.G., Tilmes, S., Emmons, L.K., Lauritzen, P.H., Walters, S., Callaghan,
871 P., Zarzycki, C.M., Barth, M.C., Jo, D.S. and Bacmeister, J.T., 2022. Evaluating the impact of
872 chemical complexity and horizontal resolution on tropospheric ozone over the conterminous US
873 with a global variable resolution chemistry model. Journal of Advances in Modeling Earth Systems,
874 14(6), p.e2021MS002889.

875 Shindell, D. T., Faluvegi, G., Stevenson, D. S., Krol, M. C., Emmons, L. K., Lamarque, J. F., et
876 al. (2006). Multimodel simulations of carbon monoxide: Comparison with observations and
877 projected near-future changes. Journal of Geophysical Research, 111.

878  Soulie, A., C. Granier, S. Darras, T. Doumbia, M. Guevara, J.-P. Jalkanen, S. Keita, C. Liousse,
879  Global anthropogenic emissions (CAMS-GLOB-ANT) for the Copernicus Atmosphere
880  Monitoring Service Air Quality Forecasts and Reanalysis, to be submitted to Earth Sys. Sci. data,
881  2023.

882  Stauffer, R.M., Thompson, A.M., Kollonige, D.E., Witte, J.C., Tarasick, D.W., Davies, J., Vömel,
883  H., Morris, G.A., Van Malderen, R., Johnson, B.J. and Querel, R.R., 2020. A post-2013 dropoff
884  in total ozone at a third of global ozonesonde stations: Electrochemical concentration cell
885  instrument artifacts?. Geophysical Research Letters, 47(11), p.e2019GL086791.

886  Stein, O., Schultz, M. G., Bouarar, I., Clark, H., Huijnen, V., Gaudel, A., et al. (2014). On the
887  wintertime low bias of Northern Hemisphere carbon monoxide found in global model simulations.
888  Atmospheric Chemistry and Physics, 14, 9295–9316.

889  Tang, W., Arellano, A. F., DiGangi, J. P., Choi, Y., Diskin, G. S., Agustí-Panareda, A., Parrington,
890  M., Massart, S., Gaubert, B., Lee, Y., Kim, D., Jung, J., Hong, J., Hong, J.-W., Kanaya, Y., Lee,
891  M., Stauffer, R. M., Thompson, A. M., Flynn, J. H., and Woo, J.-H.: Evaluating high-resolution
892  forecasts of atmospheric CO and CO2 from a global prediction system during KORUS-AQ field
893  campaign, Atmos. Chem. Phys., 18, 11007–11030, https://doi.org/10.5194/acp-18-11007-2018,
894  2018.

895  Tang, W., Emmons, L. K., Arellano Jr., A. F., Gaubert, B., Knote, C., Tilmes, S., Buchholz, R. R.,
896  Pfister, G. G., Diskin, G. S., Blake, D. R., Blake, N. J., Meinardi, S., DiGangi, J. P., Choi, Y., Woo,
897  J.-H., He, C., Schroeder, J. R., Suh, I., Lee, H.-J., Jo, H.-Y., Kanaya, Y., Jung, J., Lee, Y., and Kim,
898  D.: Source contributions to carbon monoxide concentrations during KORUS-AQ based on CAM-
899  chem     model     applications,     J.     Geophys.     Res.-Atmos.,     124,     1–27,
900  https://doi.org/10.1029/2018jd029151, 2019.

901  Tang, W., Emmons, L.K., Buchholz, R.R., Wiedinmyer, C., Schwantes, R.H., He, C., Kumar, R.,
902  Pfister, G.G., Worden, H.M., Hornbrook, R.S. and Apel, E.C., 2022. Effects of Fire Diurnal
903  Variation and Plume Rise on US Air Quality During FIREX-AQ and WE-CAN Based on the
904  Multi-Scale Infrastructure for Chemistry and Aerosols (MUSICAv0). Journal of Geophysical
905  Research: Atmospheres, 127(16), p.e2022JD036650.

906  Taylor, K. E. (2001). Summarizing multiple aspects of model performance in a single diagram.
907  Journal of Geophysical Research, 106(1755), 7183–7192. https://doi.org/10.1029/2000JD900719.

908  Thompson, A. M., Balashov, N. V., Witte, J. C., Coetzee, J. G. R., Thouret, V., and Posny, F.:
909  Tropospheric ozone increases over the southern Africa region: bellwether for rapid growth in
910  Southern     Hemisphere     pollution?,     Atmos.     Chem.     Phys.,     14,     9855–9869,
911  https://doi.org/10.5194/acp-14-9855-2014, 2014.

912  Thompson, A. M., J. C. Witte, C., Sterling, A., Jordan, B. J., Johnson, S. J. Oltmans, ... Thiongo,
913  K. (2017). First reprocessing of Southern Hemisphere Additional Ozonesondes (SHADOZ) ozone
914  profiles (1998-2016): 2. Comparisons with satellites and ground-based instruments. Journal of
915  Geophysical Research: Atmospheres, 122, 13,000-13,025. https://doi.org/10.1002/2017JD027406.

916 Thompson, C. R., Wofsy, S. C., Prather, M. J., Newman, P. A., Hanisco, T. F., Ryerson, T. B.,
917 Fahey, D. W., Apel, E. C., Brock, C. A., Brune, W. H., Froyd, K., Katich, J. M., Nicely, J. M.,
918 Peischl, J., Ray, E., Veres, P. R., Wang, S., Allen, H. M., Asher, E., Bian, H., Blake, D., Bourgeois,
919 I., Budney, J., Bui, T. P., Butler, A., Campuzano-Jost, P., Chang, C., Chin, M., Commane, R.,
920 Correa, G., Crounse, J. D., Daube, B., Dibb, J. E., DiGangi, J. P., Diskin, G. S., Dollner, M., Elkins,
921 J. W., Fiore, A. M., Flynn, C. M., Guo, H., Hall, S. R., Hannun, R. A., Hills, A., Hintsa, E. J.,
922 Hodzic, A., Hornbrook, R. S., Huey, L. G., Jimenez, J. L., Keeling, R. F., Kim, M. J., Kupc, A.,
923 Lacey, F., Lait, L. R., Lamarque, J., Liu, J., McKain, K., Meinardi, S., Miller, D. O., Montzka, S.
924 A., Moore, F. L., Morgan, E. J., Murphy, D. M., Murray, L. T., Nault, B. A., Neuman, J. A.,
925 Nguyen, L., Gonzalez, Y., Rollins, A., Rosenlof, K., Sargent, M., Schill, G., Schwarz, J. P., Clair,
926 J. M. S., Steenrod, S. D., Stephens, B. B., Strahan, S. E., Strode, S. A., Sweeney, C., Thames, A.
927 B., Ullmann, K., Wagner, N., Weber, R., Weinzierl, B., Wennberg, P. O., Williamson, C. J., Wolfe,
928 G. M., and Zeng, L.: The NASA Atmospheric Tomography (ATom) Mission: Imaging the
929 Chemistry of the Global Atmosphere, B. Am. Meteorol. Soc., 103, E761–E790, 2022.

930 Tilmes, S., Lamarque, J. F., Emmons, L. K., Kinnison, D. E., Ma, P. L., Liu, X., et al. (2015).
931 Description and evaluation of tropospheric chemistry and aerosols in the Community Earth System
932 Model (CESM1. 2). Geoscientific Model Development, 8, 1395–1426.

933 Tilmes, S., Hodzic, A., Emmons, L. K., Mills, M. J., Gettelman, A., Kinnison, D. E., et al.: Climate
934 forcing and trends of organic aerosols in the Community Earth System Model (CESM2). Journal
935 of Advances in Modeling Earth Systems, 11, https://doi.org/10.1029/2019MS001827, 2019.

936 U.S. EPA: Quality Assurance Guidance Document 2.12: Monitoring PM2.5 in Ambient Air Using
937 Designated Reference or Class I Equivalent Methods, United States Environmental Protection
938 Agency, available at: https://www3.epa.gov/ttnamti1/files/ambient/pm25/qa/m212.pdf (last
939 access: 20 November 2022), 2016.

940 van der Werf, G. R., Randerson, J. T., Giglio, L., van Leeuwen, T. T., Chen, Y., Rogers, B. M.,
941 Mu, M., van Marle, M. J. E., Morton, D. C., Collatz, G. J., Yokelson, R. J., and Kasibhatla, P. S.,
942 2017. Global fire emissions estimates during 1997–2016, Earth Syst. Sci. Data, 9, 697–720,
943 https://doi.org/10.5194/essd-9-697-2017.

944 Vohra, K., Marais, E.A., Bloss, W.J., Schwartz, J., Mickley, L.J., Van Damme, M., Clarisse, L.
945 and Coheur, P.F., 2022. Rapid rise in premature mortality due to anthropogenic air pollution in
946 fast-growing tropical cities from 2005 to 2018. Science Advances, 8(14), p.eabm4435.

947 Washington, R., Harrison, M., Conway, D., Black, E., Challinor, A., Grimes, D., Jones, R., Morse,
948 A., Kay, G. and Todd, M., 2006. African climate change: taking the shorter route. Bulletin of the
949 American Meteorological Society, 87(10), pp.1355-1366.

950 Watson, J. G., Chow, J. C., Moosmüller, H., Green, M., Frank, N., and Pitchford, M.: Guidance
951 for using continuous monitors in PM2.5 monitoring networks, U.S. EPA Office of Air Quality
952 Planning and Standards, Triangle Park, NC., 1998.

953 Wiedinmyer, C., Akagi, S.K., Yokelson, R.J., Emmons, L.K., Al-Saadi, J.A., Orlando, J.J., Soja,
954 A.J., 2011. The Fire INventory from NCAR (FINN): a high resolution global model to estimate

955  the emissions from open burning. Geosci. Model Dev. 4, 625–641. https://doi.org/10.5194/gmd-
956  4-625-2011.

957  Wiedinmyer, C., Yokelson, R. J., and Gullett, B. K.: Global emissions of trace gases, particulate
958  matter, and hazardous air pollutants from open burning of domestic waste, Environ. Sci. Technol.,
959  48, 9523–9530, https://doi.org/10.1021/es502250z, 2014.

960  Witte, J.C., A. M. Thompson, H. G. J. Smit, M. Fujiwara, F. Posny, Gert J. R. Coetzee, ... F. R. da
961  Silva (2017), First reprocessing of Southern Hemisphere ADditional OZonesondes (SHADOZ)
962  profile records (1998-2015): 1. Methodology and evaluation, J. Geophys. Res. Atmos., 122, 6611-
963  6636. https://doi.org/10.1002/2016JD026403.

964  Witte, J. C., Thompson, A. M., Smit, H. G. J., Vömel, H., Posny, F., & Stübi, R. (2018). First
965  reprocessing of Southern Hemisphere ADditional OZonesondes profile records: 3. Uncertainty in
966  ozone profile and total column. Journal of Geophysical Research: Atmospheres, 123, 3243-3268.
967  https://doi.org/10.1002/2017JD027791.

968  Worden, H. M., Deeter, M. N., Edwards, D. P., Gille, J. C., Drummond, J. R., and Nédélec, P.:
969  Observations of near-surface carbon monoxide from space using MOPITT multispectral retrievals,
970  J. Geophys. Res., 115, D18314, https://doi.org/10.1029/2010JD014242, 2010.

971  Ziervogel, G., New, M., Archer van Garderen, E., Midgley, G., Taylor, A., Hamann, R., Stuart-
972  Hill, S., Myers, J. and Warburton, M., 2014. Climate change impacts and adaptation in South
973  Africa. Wiley Interdisciplinary Reviews: Climate Change, 5(5), pp.605-620.

974

975

976

977

978
979
980
981
982

22
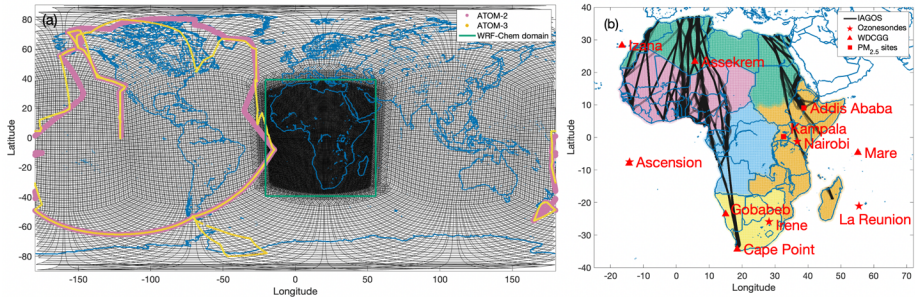
**Figure 1.** Model grid, in situ observations used in this study, and sub-regions in Africa. (a) MUSICAv0 model grid developed for Africa in this study (black), domain boundary of the WRF-Chem simulation compared in this study (shown by green box), observations from the Atmospheric Tomography Mission (ATom) field campaign 2 (ATom-2; 2017 Jan to 2017 Feb; pink) and ATom-3 (2017 Sep to 2017 Oct; yellow). (b) Sub-regions in Africa are shown, namely North Africa (green), West Africa (pink), East Africa (orange), Central Africa (blue), and Southern Africa (yellow). Location of in situ observations are labeled on the map. Flight tracks of the In-service Aircraft for a Global Observing System (IAGOS) are shown with black lines. Four ozonesonde sites are shown by pentagrams (Ascension, Irene, Nairobi, and La Reunion); six sites from the World Data Centre for Greenhouse Gases are shown by triangles (Assekrem, Cape Point, Izana, Gobabeb, Mare, and Ascension); two surface sites for $PM_{2.5}$ are shown by squares (Addis Ababa and Kampala).
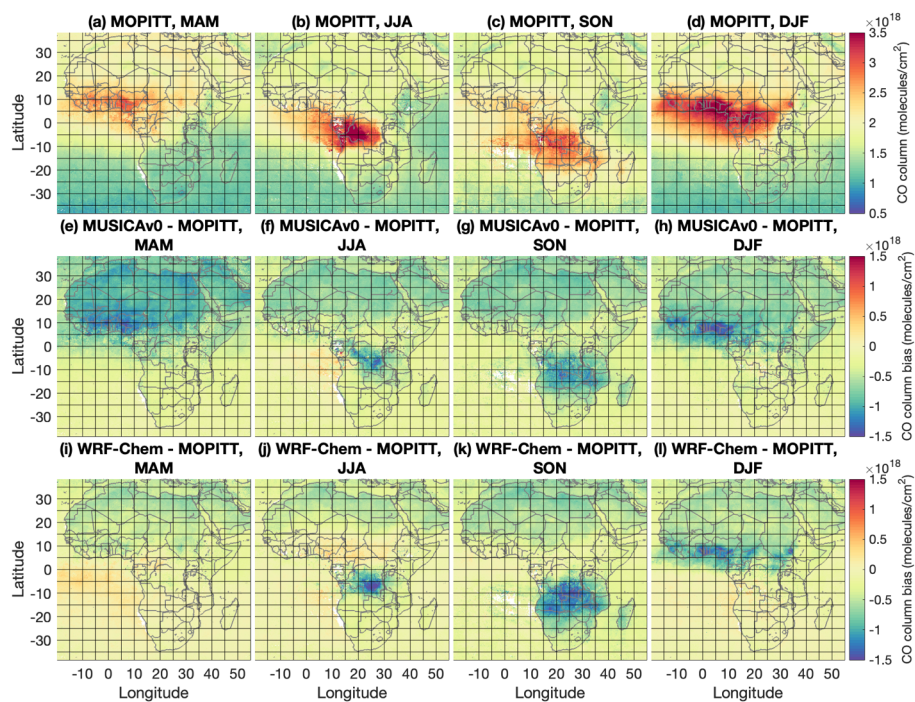
**Figure 2**. Comparisons of MUSICAv0 and WRF-Chem simulations to MOPITT CO column (molecules/cm²) for each season of 2017. (a-d) Averaged MOPITT CO column: MAM (March, April, and May), JJA (June, July, and August), SON (September, October, and November), and DJF (December, January, and February). (e-h) MUSICAv0 model biases against MOPITT CO column for MAM, JJA, SON, and DJF. (i-l) is the same as (e-h) but for WRF-Chem. All data are gridded to 0.25 degree × 0.25 degree for plotting.
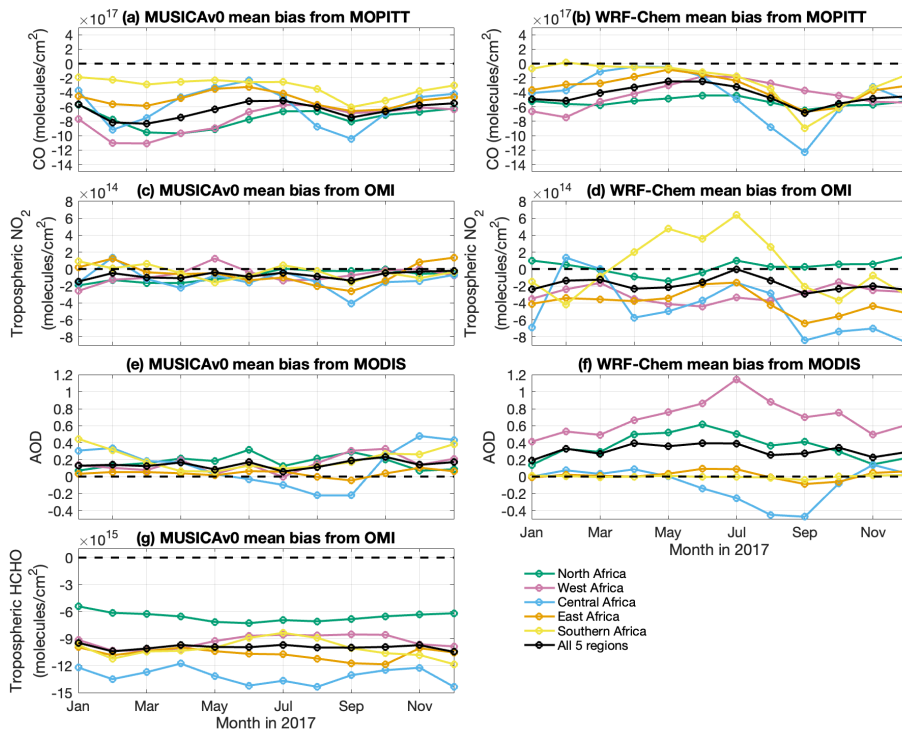
**Figure 3**. Mean bias of MUSICAv0 and WRF-Chem simulations from satellite data. Monthly timeseries of mean bias of (a) MUSICAv0 and (b) WRF-Chem against MOPITT CO column (molecules/cm$^2$) in 2017 over Africa (black), North Africa (green), West Africa (pink), East Africa (orange), Central Africa (blue), and Southern Africa (yellow). (c-d) are same as (a-b) but for mean bias against OMI tropospheric NO$_2$ column (molecules/cm$^2$). (e-f) are same as (a-b) but for mean bias against with MODIS (Terra) Aerosol Optical Depth (AOD). (g) is the same as (a) but for mean bias against OMI tropospheric HCHO column (molecules/cm$^2$).
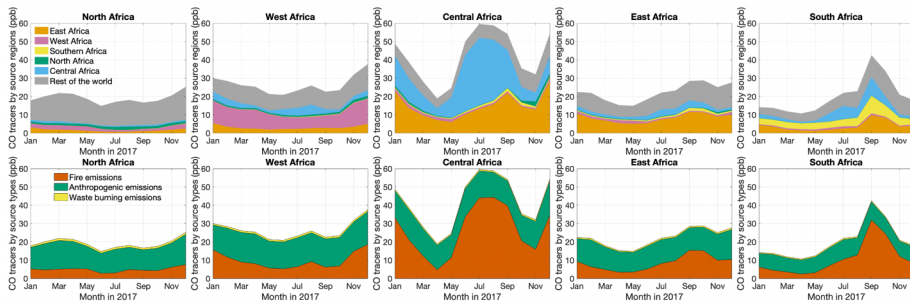
**Figure 4.** Monthly time series of column-averaged CO tracers in North Africa, West Africa, East Africa, Central Africa, and Southern Africa. Top panels show CO tracers of emissions from North Africa (green), West Africa (pink), East Africa (orange), Central Africa (blue), Southern Africa (yellow), and the rest of the world (grey). Bottom panels show CO tracers of fire emissions (red), anthropogenic emissions (green), and waste burning emissions (yellow).
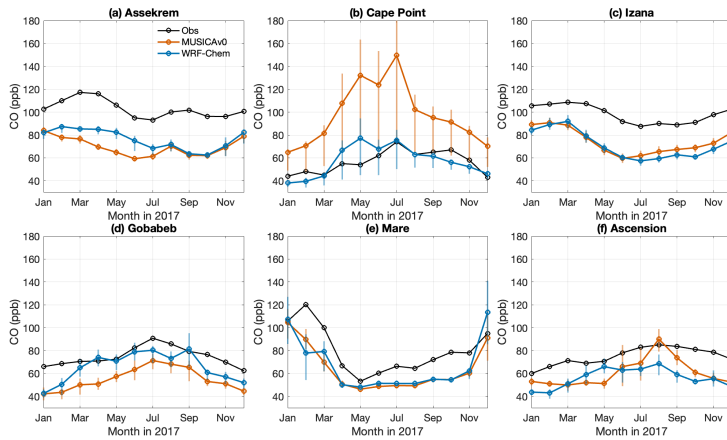


**Figure 5**. Monthly mean CO (ppb) from in situ observations (black), MUSICAv0 (red), and WRF-Chem (blue) during 2017 at (a) Assekrem, (b) Cape Point, (c) Izana, (d) Gobabeb, (e) Mare and (f) Ascension (see Figure 1b for locations). Monthly means are calculated from 3-hourly data. The range for each data point shows the variation of the 3-hourly data on that day (25% quantile to 75% quantile). Observational data are from World Data Centre for Greenhouse Gases (WDCGG).
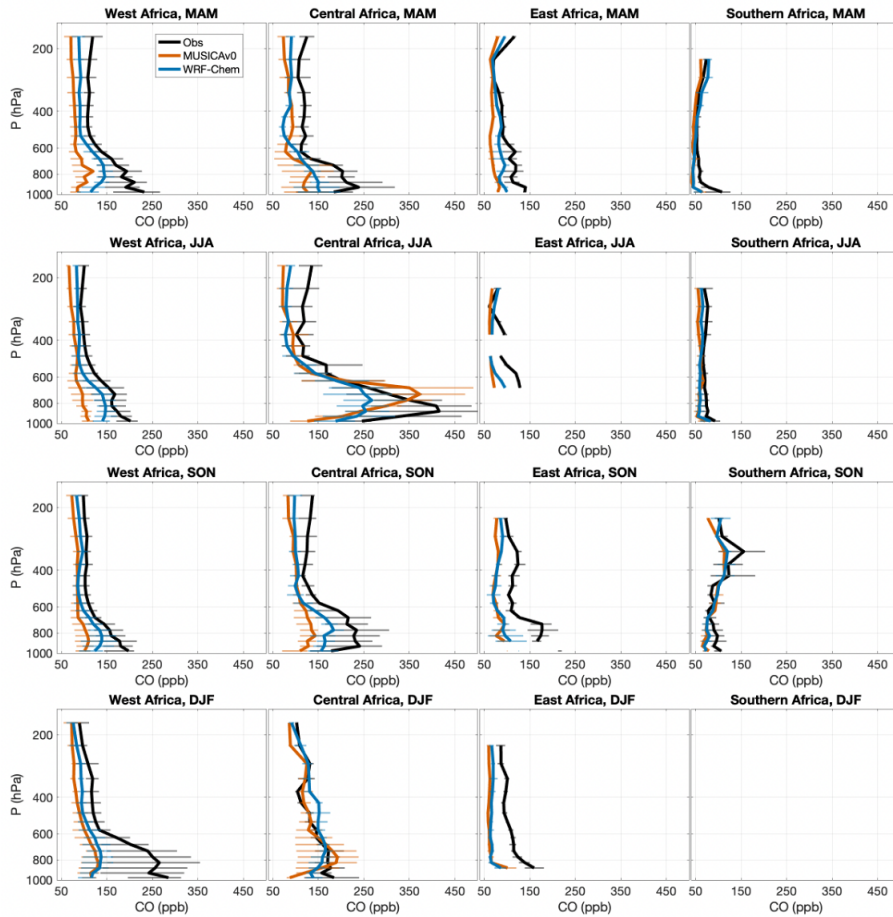
**Figure 6**. Vertical profiles of CO (ppb) from the In-service Aircraft for a Global Observing System (IAGOS) measurements (black) and corresponding model output from MUSICAv0 (red), and WRF-Chem (blue) during different seasons in 2017 over West Africa, Central Africa, East Africa, and Southern Africa. North Africa is not shown due to data availability. Seasonal mean profiles with the variation of the data in the pressure layer (25% quantile to 75% quantile) in MAM (March, April, and May), JJA (June, July, and August), SON (September, October, and November), and DJF (December, January, and February) are shown.
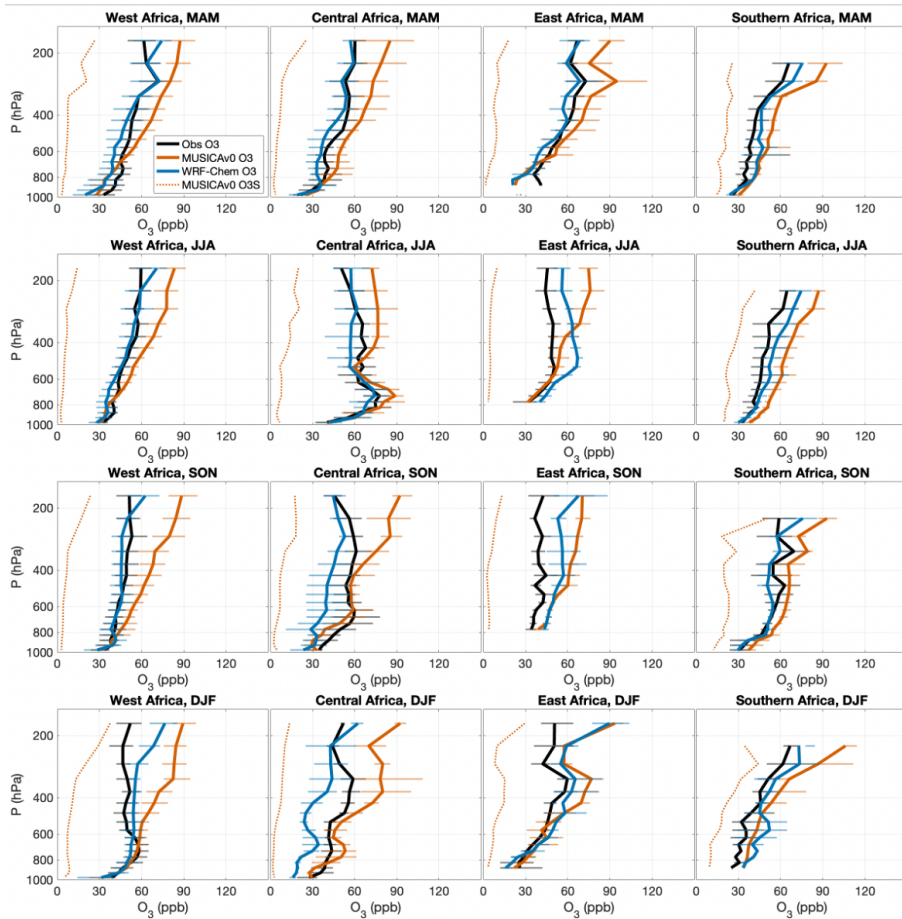
**Figure 7**. Vertical profiles of $O_3$ (ppb) from the In-service Aircraft for a Global Observing System (IAGOS) measurements (black) and corresponding model output from MUSICAv0 (red), and WRF-Chem (blue) during different seasons in 2017 over West Africa, Central Africa, East Africa, and Southern Africa. North Africa is not shown due to data availability Seasonal mean profiles with the variation of the data in the pressure layer (25% quantile to 75% quantile) in MAM (March, April, and May), JJA (June, July, and August), SON (September, October, and November), and DJF (December, January, and February) are shown. The dash red lines represent O3S (stratospheric ozone tracer) from the MUSICAv0 simulation.

28
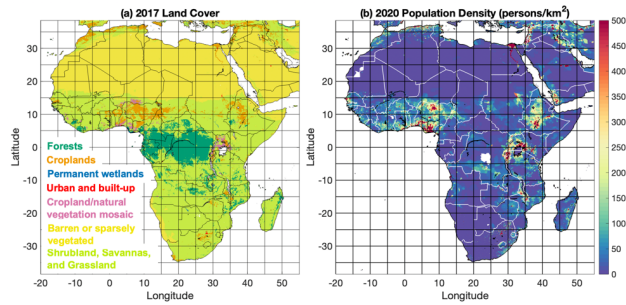
1054
1055 **Figure 8**. (a) Land cover in 2017 and (b) population density (persons/km²) in 2020 over Africa.
1056 Land cover data is from MODIS/Terra+Aqua Land Cover Type Yearly L3 Global product
1057 (resolution: 0.05 degree) (Friedl et al., 2022). Cropland/Natural Vegetation Mosaics means
1058 Mosaics of small-scale cultivation (40-60%) with natural tree, shrub, or herbaceous vegetation.
1059 Population density data is from the Gridded Population of the World, Version 4 (GPWv4),
1060 Revision 11 (CIESIN, 2018).
1061
1062

29
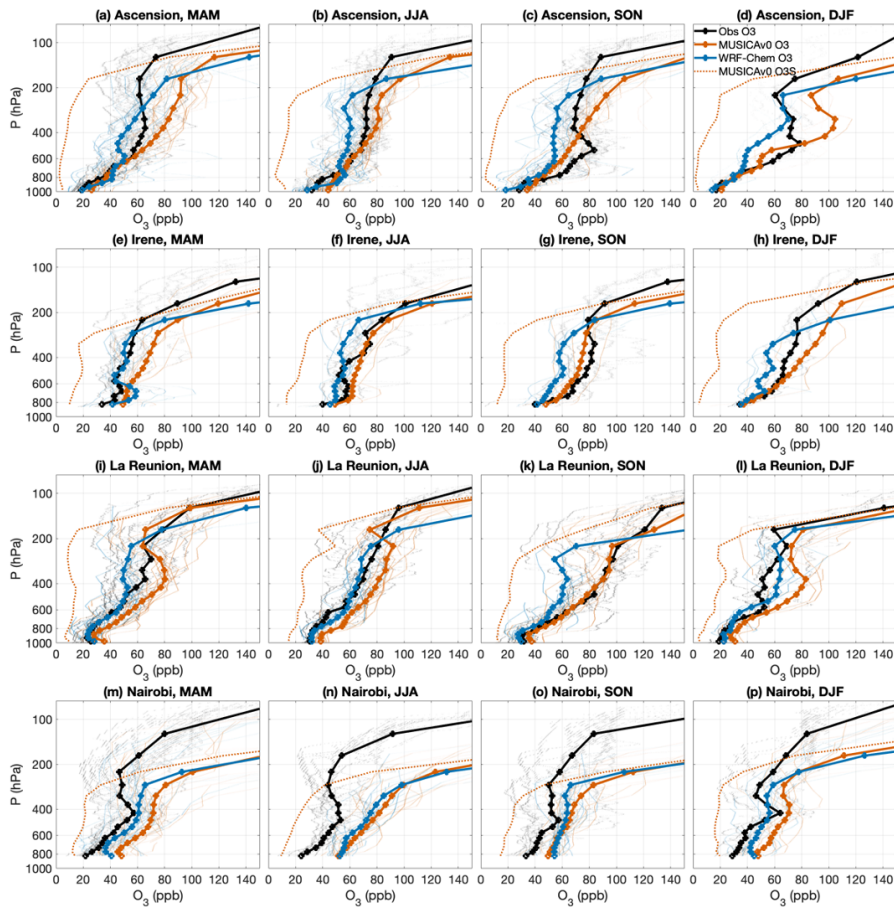
**Figure 9**. Vertical profiles of O$_3$ (ppb) from Ozonesondes (black) and corresponding model output from MUSICAv0 (red), and WRF-Chem (blue) for each season of 2017. The thick lines denote the seasonal mean profiles and the thin lines denote the individual profiles. The dash red lines represent O3S (stratospheric ozone tracer) from the MUSICAv0 simulation. Ozonesonde data at Ascension in (a) MAM (March, April, and May), (b) JJA (June, July, and August), (c) SON (September, October, and November), and (d) DJF (December, January, and February) are shown. (e-h), (i-l), and (m-p) are the same as (a-d), except for Irene, La Reunion, and Nairobi, respectively. Locations of the sites are shown in Figure 1b.
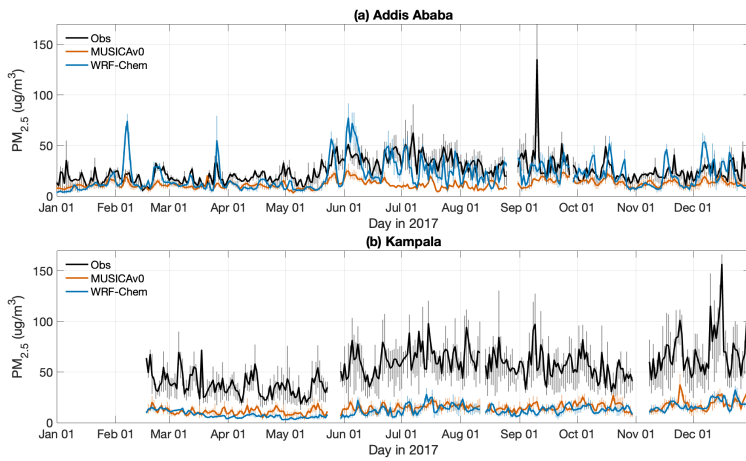
**Figure 10**. Daily mean PM$_{2.5}$ from in situ observations (black), MUSICAv0 (red), and WRF-Chem (blue) during 2017 at (a) Addis Ababa and (b) Kampala. Daily means are calculated from 3-hourly data. The shown range for each data point shows the variation on that day (25% quantile to 75% quantile). Locations of the sites are shown in Figure 1b.
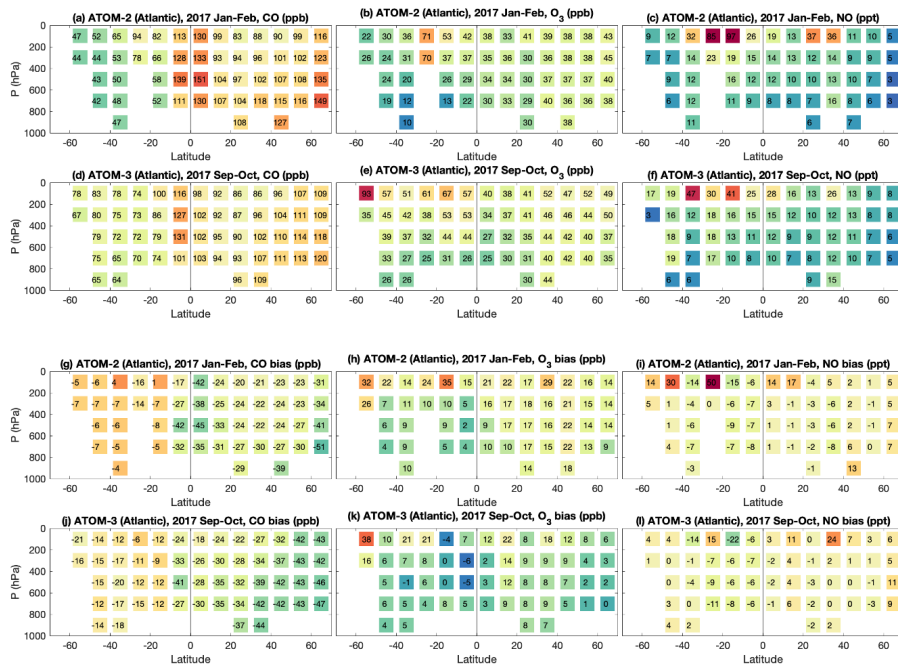
**Figure 11**. Observations of (a) CO (ppb), (b) $O_3$ (ppb), and (c) NO (ppt) over Atlantic Ocean during ATOM-2 and ATom-3 (d-f). (g-l) corresponding model biases against ATOM observations. The ATom airborne measurements and corresponding MUSICAv0 model results are binned to 10-degree latitude and 200-hPa pressure bins. The values of mean biases for each latitude and pressure bin are labeled in the figure.
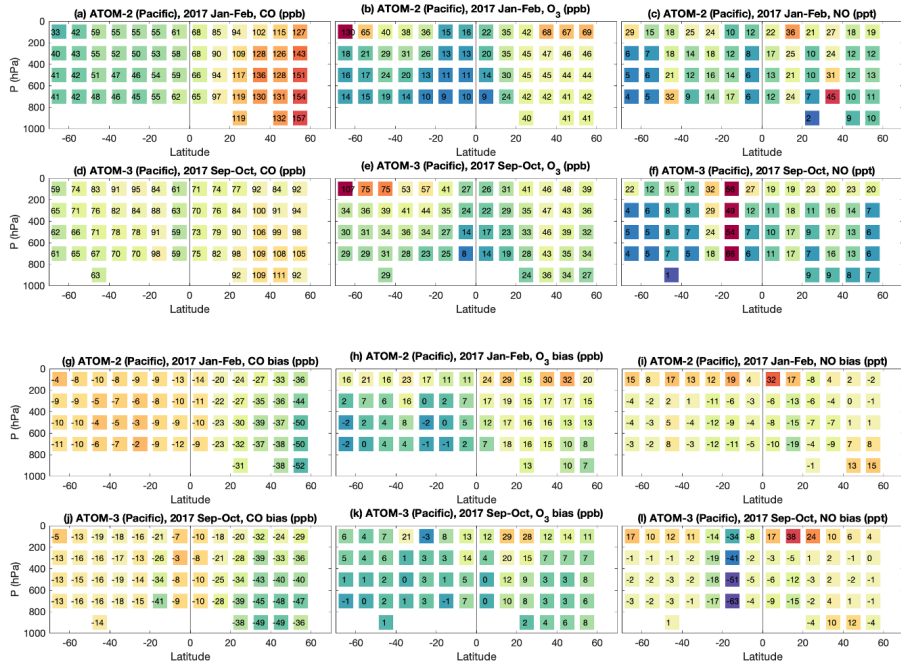
1087
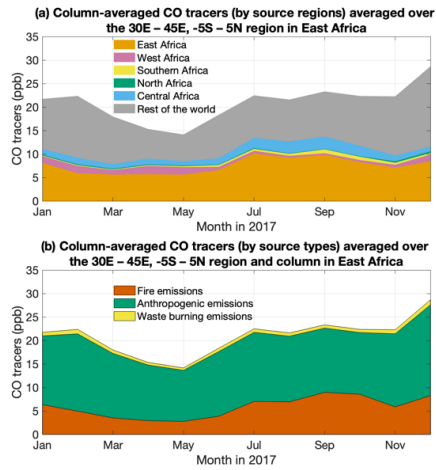1088   **Figure 12**. Same as Figure 9 but for over the Pacific Ocean.
1089
1090
1091
1092

33
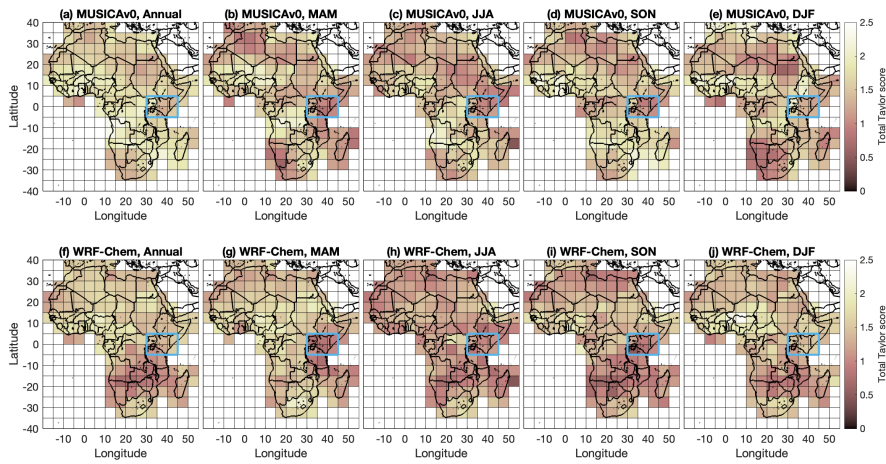
**Figure 13**. Spatial distribution of total Taylor score of MUSICAv0 and (f-j) WRF-Chem compared to satellite retrievals. In each 5° × 5° (latitude × longitude) pixel, Taylor scores of the model compared to three satellite products (e.g., MOPITT CO column retrievals, OMI tropospheric $NO_2$ column retrievals, and MODIS AOD) are calculated separately (as shown in Figure S8). Taylor score against each satellite product ranges from 0 to 1. And then three Taylor scores are summed up to obtain the shown total Taylor score (ranges from 0 to 3). Total Taylor score of MUSICAv0 for (a) 2017, (b) MAM (March, April, and May), (c) JJA (June, July, and August), (d) SON (September, October, and November), and (e) DJF (December, January, and February) are shown. The blue box highlights a potential region for future field campaigns and/or in situ observations. (f-j) are similar to (a-e) except for WRF-Chem.

**(a) Column-averaged CO tracers (by source regions) averaged over the 30E – 45E, -5S – 5N region in East Africa**

**(b) Column-averaged CO tracers (by source types) averaged over the 30E – 45E, -5S – 5N region and column in East Africa**

**Figure 14**. Monthly time series of column-averaged CO tracers in the 30°E – 45°E, -5°S – 5°N region in East Africa. (a) CO tracers of emissions from North Africa (green), West Africa (pink), East Africa (orange), Central Africa (blue), Southern Africa (yellow), and the rest of the world (grey). (b) CO tracers of fire emissions (red), anthropogenic emissions (green), and waste burning emissions (yellow).